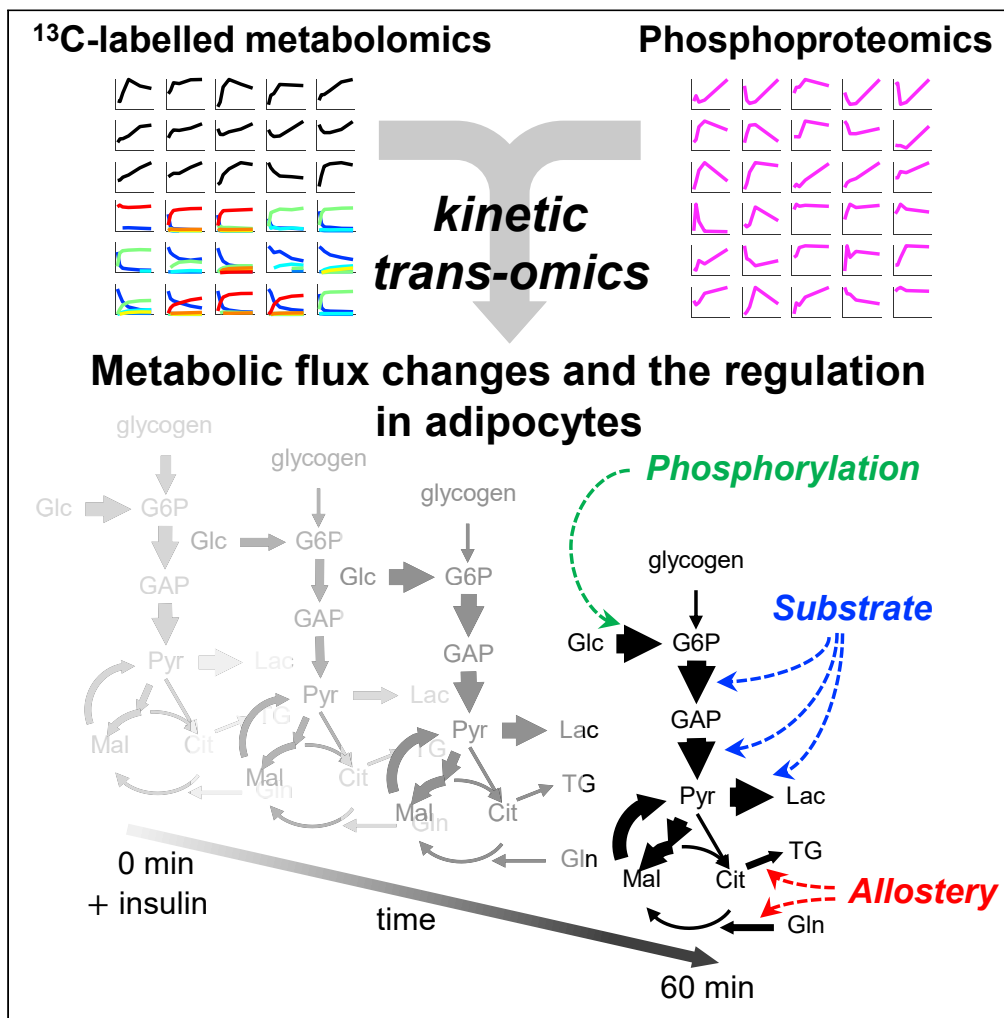


Article

# Kinetic Trans-omic Analysis Reveals Key Regulatory Mechanisms for Insulin-Regulated Glucose Metabolism in Adipocytes



Satoshi Ohno,  
Lake-Ee Quek,  
James R.  
Krycer, ...,  
Tomoyoshi Soga,  
David E. James,  
Shinya Kuroda

david.james@sydney.edu.au  
(D.E.J.)  
skuroda@bs.s.u-tokyo.ac.jp  
(S.K.)

**HIGHLIGHTS**

We developed a kinetic trans-omic network of insulin-stimulated adipocyte metabolism

Flux changes over time through the glucose metabolism were quantitatively estimated

Nine fluxes were controlled by allosteric regulation and one by phosphorylation

Key regulators were phosphorylated AS160 and the allosteric regulators of Glis and Acly



## Article

## Kinetic Trans-omic Analysis Reveals Key Regulatory Mechanisms for Insulin-Regulated Glucose Metabolism in Adipocytes

Satoshi Ohno,<sup>1,2</sup> Lake-Ee Quek,<sup>3,4</sup> James R. Krycer,<sup>3,5</sup> Katsuyuki Yugi,<sup>2,6,7,8</sup> Akiyoshi Hirayama,<sup>8,9</sup> Satsuki Ikeda,<sup>8</sup> Futaba Shoji,<sup>8</sup> Kumi Suzuki,<sup>8</sup> Tomoyoshi Soga,<sup>8,9</sup> David E. James,<sup>3,5,10,\*</sup> and Shinya Kuroda<sup>1,2,11,12,13,\*</sup>

## SUMMARY

**Insulin regulates glucose metabolism through thousands of regulatory mechanisms; however, which regulatory mechanisms are keys to control glucose metabolism remains unknown. Here, we performed kinetic trans-omic analysis by integrating isotope-tracing glucose flux and phosphoproteomic data from insulin-stimulated adipocytes and built a kinetic mathematical model to identify key allosteric regulatory and phosphorylation events for enzymes. We identified nine reactions regulated by allosteric effectors and one by enzyme phosphorylation and determined the regulatory mechanisms for three of these reactions. Insulin stimulated glycolysis by promoting Glut4 activity by enhancing phosphorylation of AS160 at S595, stimulated fatty acid synthesis by promoting Acly activity through allosteric activation by glucose 6-phosphate or fructose 6-phosphate, and stimulated glutamate synthesis by alleviating allosteric inhibition of GIs by glutamate. Most of glycolytic reactions were regulated by amounts of substrates and products. Thus, phosphorylation or allosteric modulator-based regulation of only a few key enzymes was sufficient to change insulin-induced metabolism.**

## INTRODUCTION

Cellular metabolism controls the storage of nutrients, production of energy, and synthesis of precursors of cellular components. In addition to maintaining metabolic homeostasis, cells change their metabolism in response to internal and external conditions by dynamic changes in fluxes of metabolites (Plum et al., 2006; Ray et al., 2012; Salih and Brunet, 2008). Cellular metabolism is regulated not only by the concentrations of substrates, products, and metabolic enzymes but also by acute changes in the activities of the metabolic enzymes, which are regulated by post-translational modifications of the enzymes, such as phosphorylation, as well as by allosteric effectors (Cairns et al., 2011; Kochanowski et al., 2015; Saltiel and Kahn, 2001; Yugi and Kuroda, 2017). To investigate the regulation of cellular metabolism, comprehensive studies of intracellular molecules have been conducted, using methods such as mass spectrometry (MS)-based phosphoproteomics (Humphrey et al., 2015; Jünger and Aebersold, 2014; Macek et al., 2009) and metabolomics (Hirayama et al., 2014; Peng et al., 2015; Zamboni et al., 2015). However, key regulatory mechanisms controlling cellular metabolism remain unknown, because the phosphorylation state of many proteins and the concentrations of many metabolites are dynamically changing. Together, changes in protein phosphorylation and the abundances of substrates, products, and allosteric regulators alter the activity of numerous enzymes. One approach to explore how cellular metabolism is controlled is through integration of multi-omic data with biochemical reaction data (Gerosa et al., 2015; Hackett et al., 2016; Kawata et al., 2018; Krycer et al., 2017; Yugi et al., 2014). This approach is called trans-omic analyses (Yugi et al., 2016, 2019). In previous trans-omic studies of mammalian cells responding to external hormone insulin, multi-omic data were integrated to construct qualitative trans-omic networks of hormone-induced metabolism (Kawata et al., 2018; Krycer et al., 2017; Yugi et al., 2014). However, qualitative trans-omic networks do not directly indicate how much each regulatory mechanism affects cellular metabolism. Quantitative, time-resolved, multi-omic data are required to identify the contributions of specific regulatory mechanisms to hormone-induced changes in metabolism. The temporally changing data need to be incorporated into a kinetic mathematical model that includes metabolic enzymes, their substrates, products, and allosteric

<sup>1</sup>Molecular Genetics Research Laboratory, Graduate School of Science, The University of Tokyo, Hongo 7-3-1, Bunkyo-ku, Tokyo, Japan

<sup>2</sup>Department of Biological Sciences, Graduate School of Science, The University of Tokyo, Hongo 7-3-1, Bunkyo-ku, Tokyo 113-0033, Japan

<sup>3</sup>Charles Perkins Centre, The University of Sydney, Sydney, NSW 2006, Australia

<sup>4</sup>School of Mathematics and Statistics, The University of Sydney, Sydney, NSW 2006, Australia

<sup>5</sup>School of Life and Environmental Sciences, The University of Sydney, Sydney, NSW 2006, Australia

<sup>6</sup>Laboratory for Integrated Cellular Systems, RIKEN Center for Integrative Medical Science, 1-7-22 Suehiro-cho, Tsurumi-ku, Yokohama, Kanagawa 230-0045, Japan

<sup>7</sup>PRESTO, Japan Science and Technology Agency, 1-7-22 Suehiro-cho, Tsurumi-ku, Yokohama, Kanagawa 230-0045, Japan

<sup>8</sup>Institute for Advanced Biosciences, Keio University, Tsuruoka, Yamagata 997-0052, Japan

<sup>9</sup>AMED-CREST, AMED, 1-7-1 Otemachi, Chiyoda-Ku, Tokyo 100-0004, Japan

<sup>10</sup>Sydney Medical School, The University of Sydney, Sydney, NSW 2006, Australia

<sup>11</sup>Department of Computational Biology and Medical Sciences, Graduate School of Frontier Sciences, The University of Tokyo, 5-1-5 Kashiwanoha, Kashiwa, Chiba 277-8562, Japan

<sup>12</sup>Core Research for Evolutional Science and

Continued



effectors, along with relevant phosphorylated proteins. In this study, we described trans-omic networks by kinetic equations together with time-resolved multi-omic data. We refer to this approach as kinetic trans-omic analysis. The kinetic trans-omic analysis enables identification of key regulatory mechanisms that likely influence downstream molecules from many candidate regulatory mechanisms through model selection. Moreover, the kinetic trans-omic analysis provides quantitative understanding of the relative contributions of specific regulatory mechanisms to cellular metabolism in response to key perturbations.

Insulin is a key hormone that regulates cellular glucose metabolism. Adipocytes respond to insulin by changing the flux of glucose through various metabolic pathways (Dimitriadis et al., 2011; Giorgino et al., 2005; Krycer et al., 2017, 2020b; 2020a; Quek et al., 2020). In  $^{14}\text{C}$ -glucose labeling experiments with adipocytes (Cahill et al., 1959; Katz et al., 1966), insulin increases fluxes through the metabolic pathways of glucose uptake, glycolysis, oxidative pentose phosphate (PP) pathway, glycogen synthesis, glycerol synthesis, and fatty acid synthesis. In these studies, fluxes are determined using the assumption that metabolism achieves a new steady-state condition with constant concentrations of substrates and products after insulin stimulation. However, this assumption is physiologically inaccurate particularly in the context of mammalian physiology. For example, *in vivo* insulin-stimulated changes in the fluxes through metabolic pathways are highly dynamic and are probably never at a steady state (Krycer et al., 2017, 2020a).

Various regulatory mechanisms have been reported for glucose metabolism in adipocytes or for enzymes that participate in pathways that use carbon from glucose. For example, phosphorylation controls the abundance of glucose transporter type 4 (Glut4) at the plasma membrane. Insulin stimulates glucose uptake by promoting the translocation of Glut4 into the plasma membrane (Dimitriadis et al., 2011; Giorgino et al., 2005). Akt-dependent phosphorylation of AS160, a GTPase-activating protein (GAP) for Rab GTPases, promotes Glut4 translocation into the plasma membrane. Rabs are required for the movement of Glut4 vesicles to the plasma membrane, thus phosphorylation-mediated de-inhibition of Rabs triggers Glut4 exocytosis (Huang and Czech, 2007). Once glucose is transported into the cell by Glut4, glucose flows into glycolysis. In many cell lines and organs, phosphofructokinase 1 (Pfk1) is allosterically activated by fructose 2,6-bisphosphate (F2,6BP) and inhibited by ATP and citrate (Mor et al., 2011; Passonneau and Lowry, 1963; Schöneberg et al., 2013), whereas pyruvate kinase is allosterically activated by fructose 1,6-bisphosphate (F1,6BP) and inhibited by ATP (Israelsen and Vander Heiden, 2015; Munday et al., 1980). Regulation of fatty acid synthesis is also complex. When insulin stimulates glycolysis in adipose tissue, ATP-citrate lyase (Acly) is allosterically activated by intermediates of glucose metabolism, including glucose 6-phosphate (G6P), fructose 6-phosphate (F6P), fructose 1,6-bisphosphate (F1,6BP), F2,6BP, and phosphoenolpyruvate (Potapova et al., 2000). Phosphorylation of Acly also increases the activity of the enzyme, whereas phosphorylation of fatty acid synthase (Fasn) and acetyl-CoA carboxylases 1 (Acc1) decrease their activities (Song et al., 2018).

Although many different regulatory mechanisms for enzymatic processes have been reported, many are based on experiments using different cells in different conditions or on kinetic measurements of isolated enzymes. Consequently, the relative contribution of different regulatory mechanisms to metabolic homeostasis in intact adipocytes upon insulin stimulation remains unclear. Moreover, previous reports are based on data obtained from cells or using enzymes under steady-state conditions. Little is known about the regulatory mechanisms in glucose metabolism during a dynamically changing condition such as in response to insulin (Krycer et al., 2017).

In this study, we identify the key regulatory mechanisms and the relative contributions of these events to glucose metabolism in insulin-stimulated adipocytes. We performed kinetic trans-omic analysis by developing a trans-omic network model based on kinetic equations. We selected the appropriate model with time-resolved metabolomic and phosphoproteomic data acquired under identical experimental conditions (Humphrey et al., 2013; Krycer et al., 2017; Quek et al., 2020). We performed  $^{13}\text{C}$ -metabolic flux analysis under non-steady-state conditions to estimate the dynamic changes in glucose metabolic flux using metabolomic data from  $^{13}\text{C}$ -labeling MS experiments. Using reaction kinetics, we described the estimated  $^{13}\text{C}$ -metabolic flux through each biochemical reaction. Our model includes regulation by enzyme phosphorylation, allosteric effectors, as well as the concentrations of substrates and products. With the kinetic trans-omic analysis, we identified the key regulatory mechanisms, including regulatory events and molecules, of glycolysis and fatty acid biosynthesis in insulin-stimulated adipocytes: insulin stimulated flux through glycolysis by promoting glucose transport/Glut4 translocation via phosphorylation of AS160 at

Technology (CREST), Japan Science and Technology Agency, Bunkyo-ku, Tokyo 113-0033, Japan

<sup>13</sup>Lead Contact

\*Correspondence:  
david.james@sydney.edu.au  
(D.E.J.),  
skuroda@bs.s.u-tokyo.ac.jp  
(S.K.)

<https://doi.org/10.1016/j.isci.2020.101479>

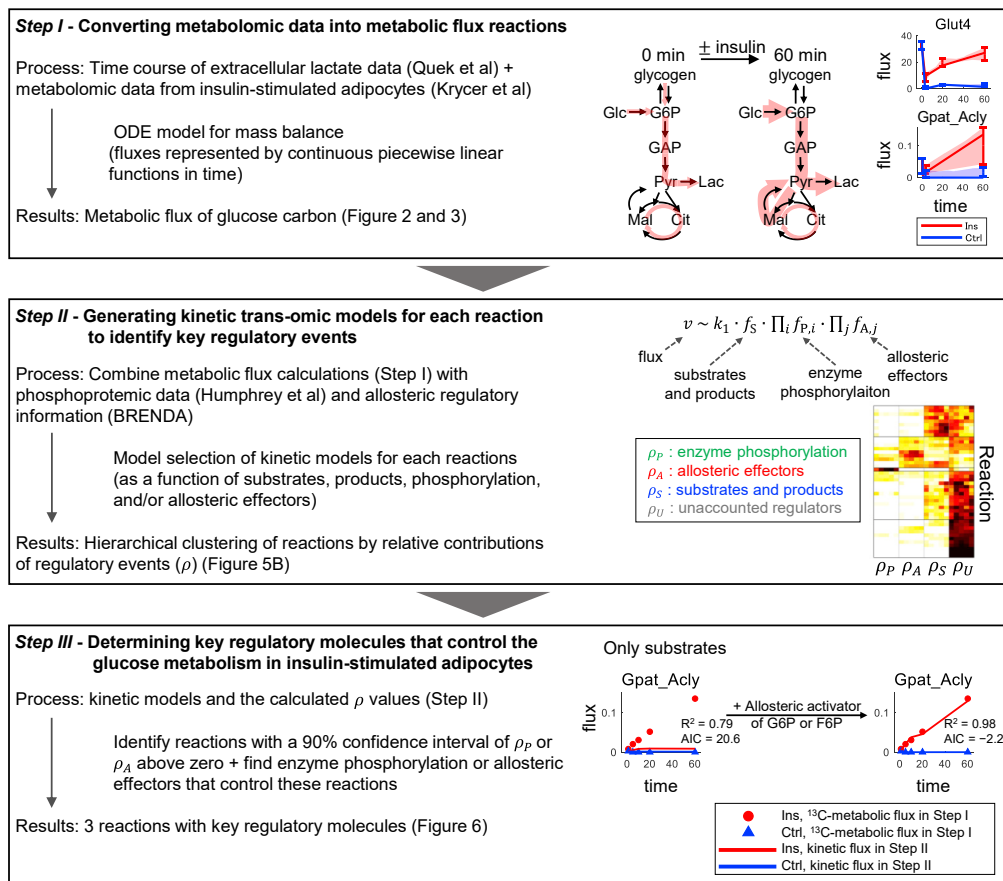


**Figure 1. Summary of Kinetic Trans-omic Analysis to Identify Key Regulatory Mechanisms in Insulin-Stimulated Adipocytes**

The procedures consist of three steps by integrating  $^{13}\text{C}$ -labeled metabolic data and phosphoproteomic data together with kinetic mathematical modeling.

S595. Insulin stimulated flux through Gpat\_Acly by allosteric activation by G6P or F6P. Insulin stimulated flux through glutaminase by alleviating allosteric inhibition by glutamate. Our analysis indicated that most glycolytic reactions were regulated by amounts of substrates and products rather than by changes in phosphorylation or by allosteric effectors. Thus, with experimental and modeling approaches, our kinetic trans-omic analysis demonstrates the importance of taking a holistic approach to understand how protein modifications and metabolite regulators work in a dynamically changing complex biochemical network.

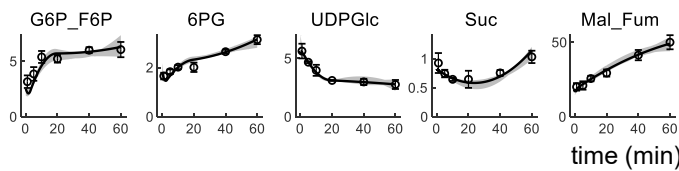
## RESULTS

### Overview of Kinetic Trans-omic Analysis

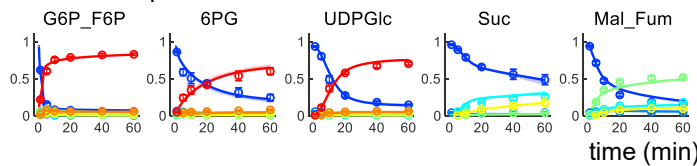
Here, we developed a kinetic trans-omic analysis and identified the key regulatory mechanisms, such as changes in enzyme phosphorylation, allosteric effectors, substrates, and products, for glucose metabolic flux in insulin-stimulated adipocytes (Figure 1). The cells used for the analysis were mouse 3T3-L1 cells differentiated into adipocytes (Green and Kehinde, 1975). The kinetic trans-omic analysis consisted of the following three steps. *Step I*: we used mass balances in the metabolic network to model flux changes from studies of adipocytes treated with or without insulin (Krycer et al., 2017; Quek et al., 2020). The data were from time-resolved  $^{13}\text{C}$ -labeled metabolomic data and extracellular lactate studies; *Step II*: we developed a kinetic trans-omic model using phosphoproteomic data (Humphrey et al., 2013) and information from a database of allosteric regulators (Placzek et al., 2017) and quantified the contribution of regulatory events mediated by enzyme phosphorylation, allosteric effectors, substrates, and products to the observed changes in metabolic flux; *Step III*: we identified key regulatory molecules involving

## Ins

### Metabolite concentrations (nmol/mg-protein)

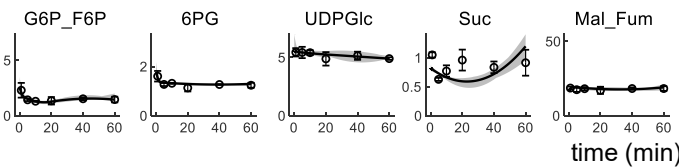


### Mass isotopomer fractions



## Ctrl

### Metabolite concentrations (nmol/mg-protein)



### Mass isotopomer fractions

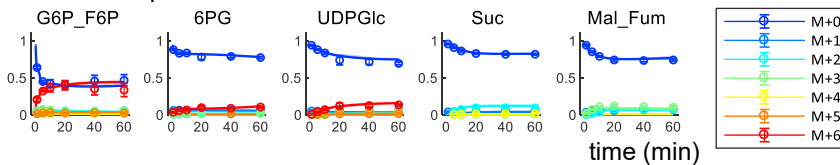


**Figure 2. Measured and Estimated Metabolic Concentrations and Mass Isotopomer Fractions in the Ins and Control Ctrl Conditions**

The circles and the error bars indicate the mean and the standard deviations of the measurements from three separate experiments (Krycer et al., 2017). The lines and the shaded areas indicate optimal estimates with the 90% confidence intervals for the values calculated with the model. M + *i* indicates mass isotopomer with *i* carbons labeled with <sup>13</sup>C. Note that media were exchanged at 0 min in both conditions. All measured and estimated metabolites concentrations and their mass isotopomer fractions are shown in Figure S2, metabolites are defined in Table S1, and estimated concentrations are shown in Table S2 and Data S1.

phosphorylation of specific proteins or specific allosteric effectors that control flux through insulin-regulated reactions.

### Step I: Converting Metabolomic Data into Metabolic Flux Reactions

We calculated glucose metabolic flux changes in insulin-stimulated adipocytes using <sup>13</sup>C-metabolic flux analysis under non-steady state (Figure S1). We used <sup>13</sup>C-labeled metabolomic data (Krycer et al., 2017) and extracellular lactate data (Quek et al., 2020) from adipocytes with (Ins) or without insulin (Ctrl) stimulation (Figures 2 and S2 and Data S1A). Adipocytes were exposed to medium containing [U-<sup>13</sup>C]glucose-containing media in the presence or absence of 100 nM insulin. Intracellular metabolites labeled with <sup>13</sup>C were quantified by MS at six time points over a total of 60 min.

For the Ins and Ctrl samples, we calculated flux changes from the metabolite concentrations and mass isotopomer fractions using an ordinary differential equation (ODE) model for mass balance with fluxes represented by continuous piecewise linear functions in time (Figure S1, see Transparent Methods). Briefly, we defined reaction stoichiometry and carbon atom transitions in glucose metabolism (Table S1) and developed an ODE model for mass balance of the intracellular metabolites and their mass isotopomers. Some of the adjacent metabolites and their isotopic ratios, such as G6P and F6P, and malate and fumarate,

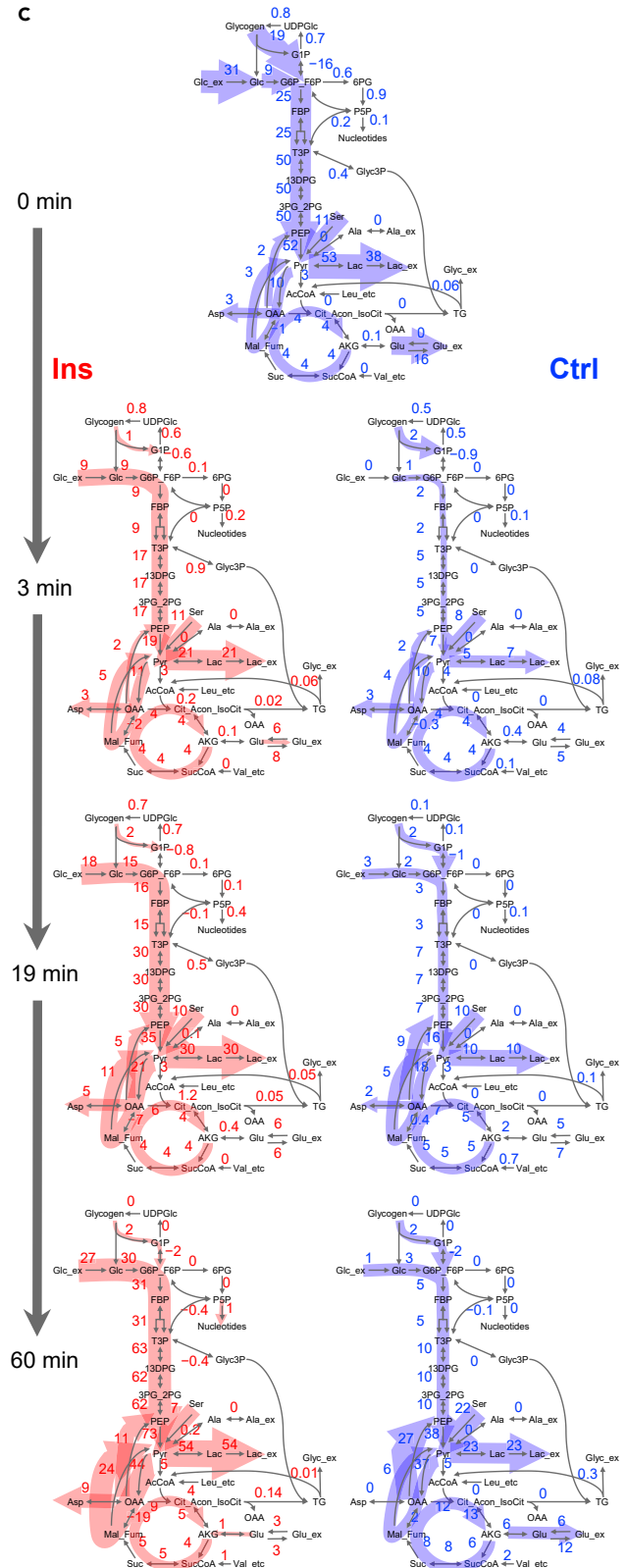
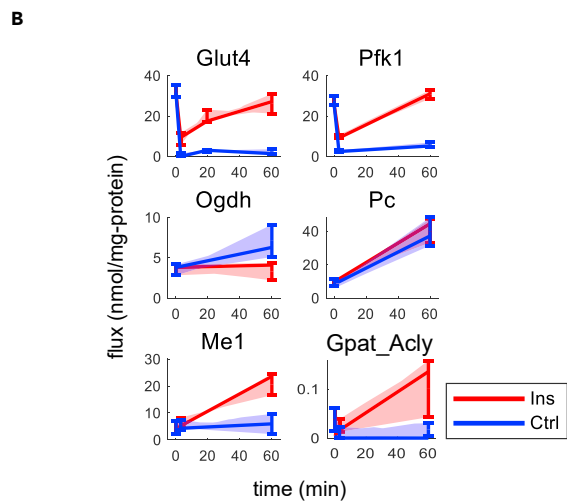
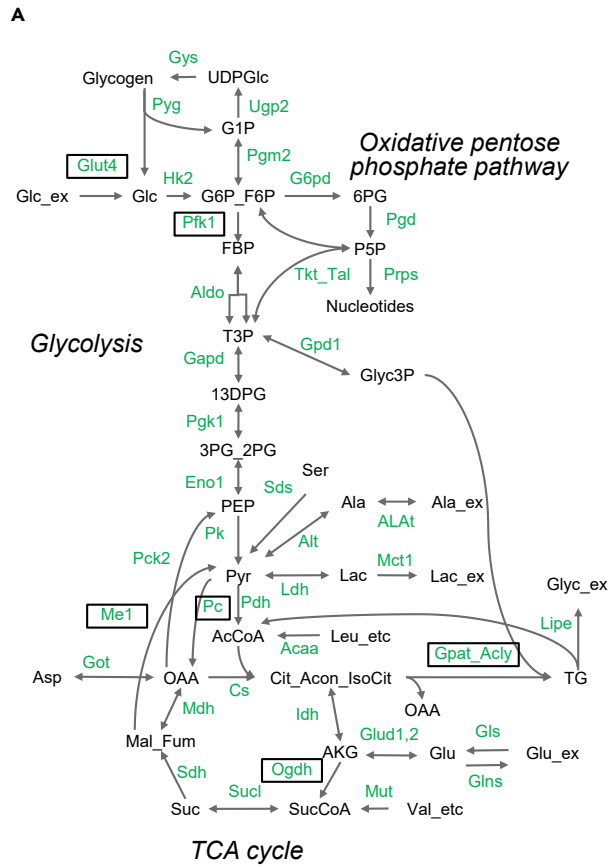


### Figure 3. Metabolic Flux Changes in Glucose Metabolism in Adipocytes With or Without Insulin Stimulation

(A) Metabolic network used for metabolic flux analysis. Green characters besides arrows are abbreviations of enzymes or proteins that mediate the reactions (see Table S1 for definitions). Reactions shown in (B) are boxed. Reactions for NADH oxidation, NADPH oxidation, and CO<sub>2</sub> transport are not shown but are included in the model for metabolic flux analysis

(B) Estimated flux changes over time through representative reactions of Glut4, Pfk1, Ogdh, Pc, Me1, and Gpat\_Acly. The lines and the shaded areas indicate optimal estimates with the 90% confidence intervals. The error bars indicate the 90% confidence intervals at switch times (times when the slope of flux changes), as well as at 0 and 60 min. Different number of time intervals (and switch times) were set among reactions (see Transparent Methods, Figure S1). The confidence intervals were calculated from 200 sets of sampled parameters under constraints based on the covariance matrix of the estimated parameters (see Transparent Methods), and the optimal estimates can be outside the confidence intervals. Fluxes at 0 min between the Ins and Ctrl conditions are set to be the same. All estimated flux changes are shown in Figure S3 and Table S2.

(C) Changes in fluxes in glucose metabolism in adipocytes in the Ins and Ctrl conditions. Numbers besides reactions are the optimal estimates of fluxes with the unit of nmol/mg-protein/min. The thickness of the red or blue shading indicates the relative flux. Fluxes between 2-oxoglutarate (AKG) and glutamate (Glu) are the summation of fluxes through NADH-dependent glutamate dehydrogenase, NADPH-dependent glutamate dehydrogenase, alanine aminotransferase, and aspartate aminotransferase. The negative value of the flux represents backward direction of the reaction, and the direction is defined in Table S1.

See also Figures S3, S6, and S7, Tables S1 and S2, and Data S1.

were similar (Figure S2). Therefore, we considered these metabolites to be in rapid equilibrium and summed them as one metabolite, G6P\_F6P and Mal\_Fum, in the model (Figure 3A, Table S1). For those metabolites that were not measured, such as pyruvate (Pyr) and succinyl-CoA (SucCoA), we used the model to predict their concentrations and mass isotopomer fractions (Figure S2). To represent the non-steady-state nature of the system, we described fluxes as continuous piecewise linear functions in the time domain (Abate et al., 2012; Leighty and Antoniewicz, 2011) (Figure S1). This approach enabled representation of flux changes without using reaction kinetics. Because adipocytes were stimulated with insulin at 0 min, the metabolite concentrations and metabolic fluxes at 0 min in both the Ins and Ctrl conditions were set at the same values. We then calculated optimal flux changes in the Ins and Ctrl conditions (Figure S3, Table S2). To obtain optimal flux changes, we minimized variance-weighted residual sum of squared errors between measured concentrations and mass isotopomer fractions of metabolites and those predicted by the model. Metabolite concentrations and mass isotopomer fractions were highly correlated between measurements and predictions (Figures 2 and S2), indicating that metabolite concentrations and mass isotopomer fractions are reasonably explained by the model.

Insulin increased fluxes through Glut4 and glycolysis (Figures 3A–3C). Flux through Pfk1 (Figures 3A–3C) in glycolysis increased from 9 nmol/mg-protein/min at 3 min to 31 nmol/mg-protein/min at 60 min in the Ins condition, whereas it remained relatively steady (2–5 nmol/mg-protein/min) between these times in the Ctrl condition. Thus our metabolic flux model indicates that the flux through Pfk1 in glycolysis was markedly increased by insulin stimulation, which is consistent with previous findings (Cahill et al., 1959; Katz et al., 1966). Decreased flux through Glut4 and Pfk1 from 0 to 3 min in both the Ins and Ctrl conditions is likely due to the effect of media change, because fluxes through Glut4 and Pfk1 decreased similarly in both Ins and Ctrl conditions (Quek et al., 2020).

In the Ins condition, fluxes through pyruvate carboxylase (Pc) and malic enzyme 1 (Me1) (Figures 3A–3C) increased over time, resulting in a flux cycle between malate and fumarate on one side and pyruvate on the other. At 60 min in the Ins condition, flux through this cycle became larger than the flux through the tricarboxylic acid (TCA) cycle (Figure 3C). In contrast to the flux cycle through Pc and Me1, fluxes through oxidative TCA cycle in the TCA cycle in the Ins condition did not change (Figure 3C). This result indicates that insulin does not have a large influence on fluxes through oxidative TCA cycle.

Fluxes through oxidative PP pathways were less than 2 nmol/mg-protein/min (Figure 3C) in both the Ins and Ctrl conditions. The oxidative PP pathway produces NADPH for reducing power in cells. In the Ins condition, the flux through oxidative PP pathway was much smaller than flux through Me1, which also produces NADPH. Thus, our results are consistent with a previous study showing that insulin-stimulated adipocytes generate most of their cellular reducing power from the Me1 reaction, rather than the oxidative PP pathway (Liu et al., 2016).

Insulin stimulated fluxes through triacylglycerol (TG) biosynthesis (Figures 3A–3C). We represented this process as a merged reaction, Gpat\_Acly, consisting of glycerol-3-phosphate acyltransferase (Gpat) and Acly (see Transparent Methods). Stimulation of TG biosynthesis is a well-known action of insulin (Cahill et al., 1959; Dimitriadis et al., 2011; Giorgino et al., 2005; Katz et al., 1966). Note that reactions of Gpat

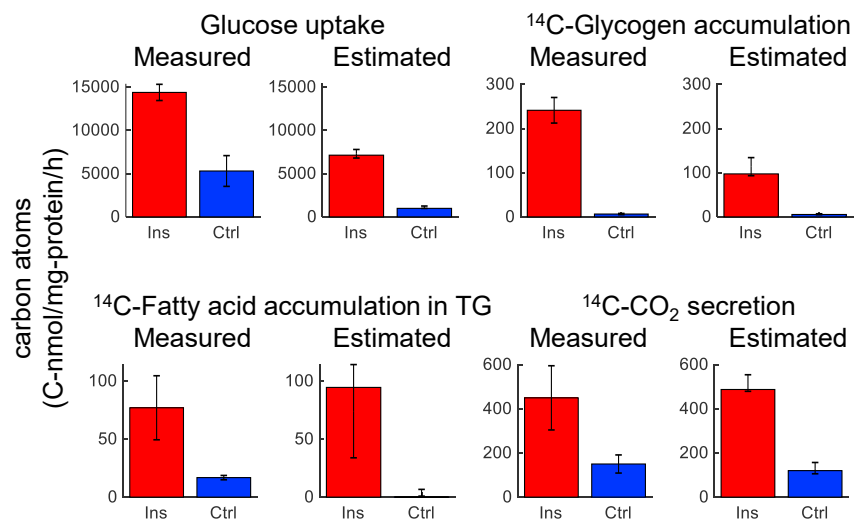


**Figure 4. Validation of the Estimated Flux with Experimental Data Using <sup>14</sup>C-Glucose**

Error bars indicate 90% confidence intervals for the measurements and the estimates. The 90% confidence intervals for the measurements were calculated by the means  $\pm z \times$  the standard errors, where  $z$  is the Z score for 90% confidence intervals (1.6449). Estimated amounts were obtained by integrating sum of products of corresponding fluxes and mass isotopomer fractions of precursor metabolites (see [Transparent Methods](#)).

and Acly were merged as one reaction in our metabolic network to maintain the stoichiometric flux balance from glycerol 3-phosphate and citrate to TG (see [Transparent Methods](#)). The synthesis of fatty acids in TG requires considerable NADPH molecules. Our model predicted that these were derived primarily from increased flux through the Me1 reaction ([Figures 3B and 3C](#)). Notably, the intracellular level of NADPH remained stable in both the Ins and Ctrl cells ([Figure S2](#)). Thus, our model indicated that insulin stimulated an increase in glucose flux through Me1 to meet the NADPH demand for insulin-stimulated TG synthesis.

We validated the flux predictions from the model with alternate experiments using natural glucose or <sup>14</sup>C-glucose as a tracer ([Quek et al., 2020](#)). These data were not used to generate the model to calculate flux. We used the model to predict fluxes involved in glucose uptake, <sup>14</sup>C-glycogen accumulation, <sup>14</sup>C-fatty acid accumulation in TG, and <sup>14</sup>C-CO<sub>2</sub> secretion and compared those predictions with the experimental data ([Figure 4](#)). In both the model and the experiments, insulin stimulated glucose uptake, <sup>14</sup>C-glycogen accumulation, <sup>14</sup>C-fatty acid accumulation in TG, and <sup>14</sup>C-CO<sub>2</sub> secretion. The measured and calculated fluxes for each of these reactions were of a similar order of magnitude, indicating that the model is sufficiently accurate to use to quantitatively identify key regulatory events.

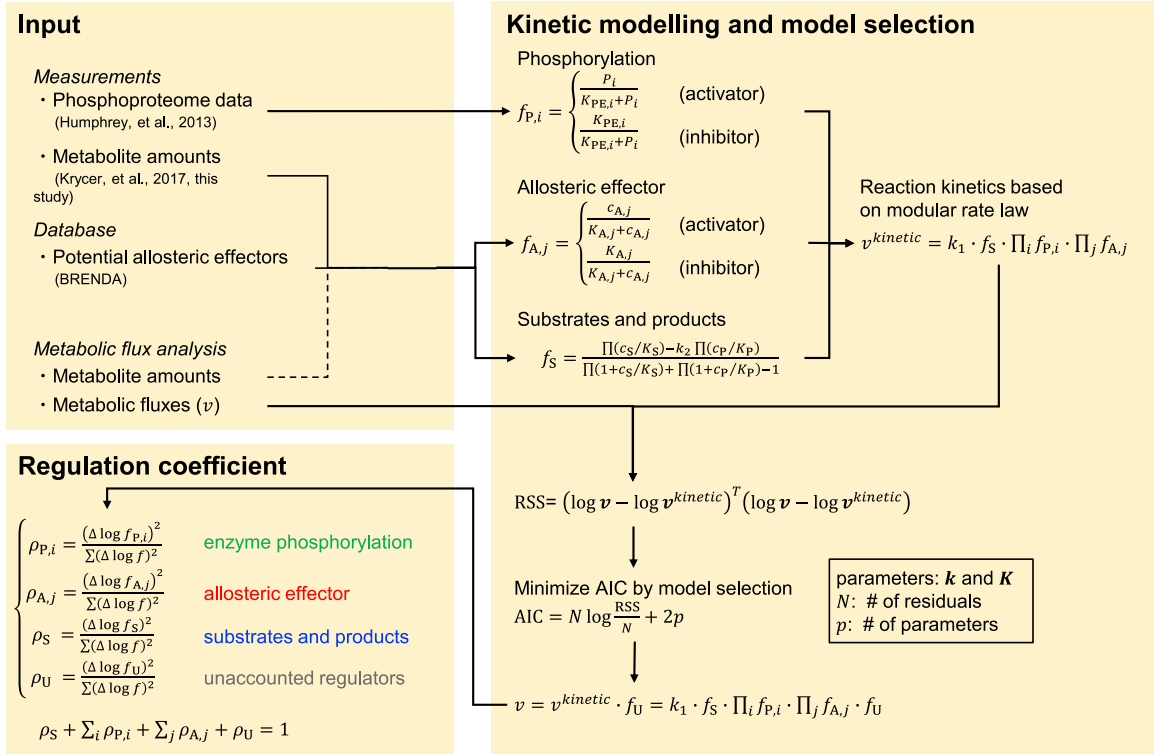
## Step II: Generating Kinetic Trans-omic Models for Each Reaction to Identify Key Regulatory Events

Time-resolved metabolomic and phosphoproteomic data implicitly represent quantitative information of regulation of fluxes by changes in enzyme phosphorylation, allosteric effectors, substrates, and products. To quantify the contributions of these regulatory events to the differences in the predicted fluxes between the Ins and Ctrl conditions, we used time-resolved metabolomic and phosphoproteomic data acquired under the same conditions ([Figure 5](#)). We developed kinetic models for each flux using modular rate law ([Liebermeister et al., 2010](#)) ([Figure 5A](#)).

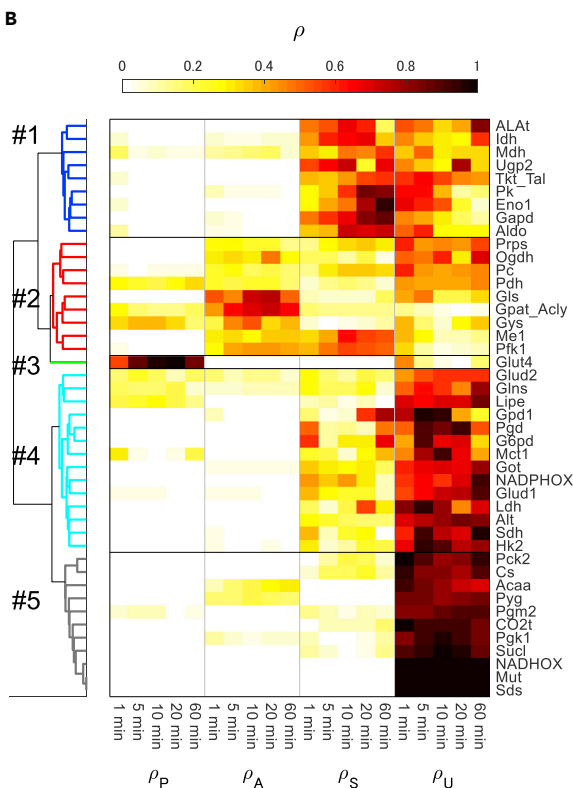
In the modular rate law, flux is defined as a product of the kinetic constant  $k_1$  and a function for the amounts of substrates and products, and other functions for enzyme phosphorylation and allosteric effectors. We assumed that enzyme amounts remained constant during the 60 min after insulin stimulation. We believe that this is a valid assumption because the duration of the experiments was much shorter than the 31-h median half-life of proteins ([Sandoval et al., 2013](#)). The enzyme amounts were implicitly included in  $k_1$ . We used the amounts of substrates and products from metabolomic data in adipocytes with or without insulin stimulation ([Krycer et al., 2017](#)). If the data were not available, we used the calculated amounts from our



A



B



C

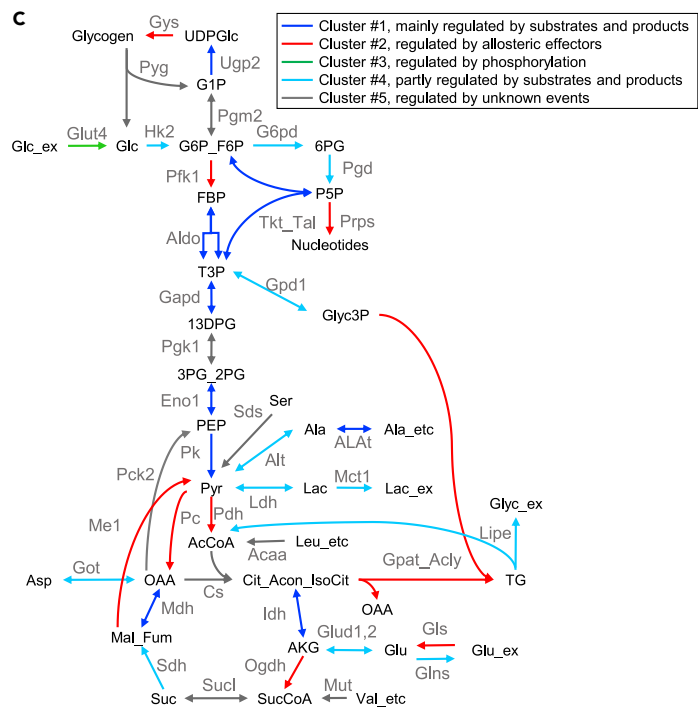


**Figure 5. Key Regulatory Events by Enzyme Phosphorylation, Allosteric Effectors, Substrates, and Products**

(A) Overview of the method for quantifying the contribution of regulatory events. Delta ( $\Delta$ ) indicates difference between the Ins and Ctrl conditions. (B) Clustering of reactions by key regulatory events. Hierarchical clustering was performed on regulation coefficients of  $\rho_P$ ,  $\rho_A$ ,  $\rho_S$ , and  $\rho_U$  at 1, 5, 10, 20, and 60 min using Euclidean distance as a metric with the Ward method. The data matrix used for the clustering contains 44 rows for reactions and 4,020 columns (5 time points  $\times$  4  $\rho$   $\times$  201 optimal and sampled parameters) (Table S4), and the mean of  $\rho$  among optimal and sampled parameters is shown as color in the heatmap. See Figures S4A and S8, Tables S3 and S4, and Data S1. (C) The metabolic network shown with each reaction colored according to its cluster classification.

metabolic flux analysis (Figure S2). We also used the enzyme phosphorylation sites and the amounts of the phosphorylation from phosphoproteomic data in insulin-stimulated adipocytes (Humphrey et al., 2013). Metabolites, as potential allosteric effectors for the corresponding metabolic enzymes, were identified from the BRENDA database (Placzek et al., 2017), and their amounts were obtained from metabolomic data with or without insulin stimulation (Krycer et al., 2017), or from the amounts calculated in our metabolic flux analysis (Figure S2). All phosphorylation sites and allosteric effectors are listed in Table S3. Kinetic parameters in the modular rate law were calculated by minimizing residual sum of squared errors between the fluxes defined by the modular rate law and the  $^{13}\text{C}$ -metabolic fluxes calculated from metabolic flux analysis (see Transparent Methods).

In our trans-kinetic model with 44 reactions, we identified 82 candidate phosphorylation sites (80 unique sites on 25 enzymes) and 170 candidate allosteric effectors for 35 reactions (Table S3). To determine the contributions of each phosphorylation, allosteric effector, and substrate and product to the fluxes, we modeled the 44 reactions with and without phosphorylation and allosteric effectors, and performed model selection using a stepwise selection method based on Akaike's Information Criterion (AIC) (Burnham et al., 2011; Yamashita et al., 2007). With this model selection, we identified enzyme phosphorylation and allosteric effectors, which gives a better representation of  $^{13}\text{C}$ -metabolic flux by reaction kinetics (Figure 5A, see Transparent Methods). Briefly, we developed models of each reaction in which the modular rate law contained  $k_1$ , and a function for substrate and product, along with a function for phosphorylation, a function for allosteric effectors, or a function for both phosphorylation and allosteric effectors. We performed stepwise model selection for each reaction independently using optimal flux predictions from the metabolic flux analysis and selected the model with the smallest AIC for each reaction. The model finally selected represents regulatory events by substrates, products, and the selected enzyme phosphorylation and/or allosteric effectors.

We next quantified contributions of the regulatory events to the differences in the predicted fluxes between the Ins and Ctrl conditions by defining a regulation coefficient  $\rho$  for each regulatory event: enzyme phosphorylation ( $\rho_P$ ), allosteric effectors ( $\rho_A$ ), substrates and products ( $\rho_S$ ), and unaccounted regulators ( $\rho_U$ ). The sum of all  $\rho$  equals 1, and a larger  $\rho$  indicates a larger contribution to flux at each time point. We calculated  $\rho$  values and the confidence intervals for all 44 reactions at each time point (Figure S4A, Table S4).

To reveal patterns of regulation and to identify key regulatory events in glucose metabolism in insulin-stimulated adipocytes, we performed hierarchical clustering analysis based on the calculated  $\rho$  at each time point. Such analysis resulted in five clusters for the 44 reactions (Figures 5B and 5C). Two clusters contain reactions primarily regulated by either phosphorylation or allosteric effectors. Cluster #3 contains only one reaction, Glut4, a rate-limiting reaction for glucose uptake. This is the only reaction with a large  $\rho_P$ , indicating that flux through this reaction is regulated by phosphorylation. Cluster #2 is characterized by reactions with larger  $\rho_A$ , indicating that fluxes through these reactions are regulated by allosteric effectors. Cluster #2 contains nine reactions, including Gpat\_Acly, glutaminase (Gls), and glycogen synthase (Gys), which are associated with synthesis or degradation of cellular macromolecules (lipid, protein, and glycogen, respectively). This cluster also includes Pc and Me1, which are reactions that replenish intermediates in the TCA cycle.

Two clusters contain reactions primarily or partially regulated by changes in substrates and products (Figures 5B and 5C). Cluster #1 is characterized by reactions with large  $\rho_S$  values, indicating that fluxes through these reactions are mainly regulated by substrates and products. Cluster #1 contains many reactions in glycolysis, including aldolase (Aldo), glyceraldehyde-3-phosphate dehydrogenase (Gapd), enolase 1 (Eno1), and pyruvate kinase (Pk). This result indicates that most glycolytic fluxes were regulated by changes in the amounts of substrates and products rather than phosphorylation or allosteric regulation. Cluster #4 is characterized by a high  $\rho_U$ , indicating unknown regulation, and a moderate  $\rho_S$ , indicating that fluxes

through these reactions are partly regulated by substrates and products. Cluster #5 is characterized by large  $\rho_U$ , and the mechanism for regulation of flux through these reactions are mostly unknown.

This analysis revealed key regulatory events in glucose metabolism in insulin-stimulated adipocytes. Among the 44 reactions in glucose metabolism, insulin regulated only nine reactions (20%, Cluster #2) primarily through allosteric effectors and only one reaction (2%, Cluster #3) primarily through phosphorylation. Changes in the amounts of substrates and products had a large effect on nine reactions (20%, Cluster #1) and a partial effect on 14 reactions (32%, Cluster #4). Eleven reactions (25%, Cluster #5) had unknown mechanisms of regulation by insulin.

To assess the accuracy of our modeling, we compared the calculated Michaelis-Menten constants in this study with the experimental values from BRENDA (Placzek et al., 2017). We used reactions with time-averaged  $\rho_U$  smaller than 0.5 because the fluxes of these reactions were well explained by known regulation by substrates, products, and, where appropriate, enzyme phosphorylation or allosteric effectors. We compared 20 estimated  $K_S$  and  $K_P$  values with  $K_M$  values in BRENDA and found that these values showed positive correlation (Pearson's correlation coefficient = 0.47,  $p = 0.036$ ) (Figure S4B), supporting reasonable accuracy of parameter estimation.

### Step III: Determining Key Regulatory Molecules that Control the Glucose Metabolism in Insulin-Stimulated Adipocytes

To select the reactions to investigate in detail for regulation by phosphorylation or allosteric effectors, we calculated the average  $\rho$  values for each regulatory event over the entire 60 min time course (Figure S5A). We selected reactions for which  $\rho_P$  or  $\rho_A$  had a 90% confidence interval above zero. Only three reactions met these criteria: Glut4 with a time-averaged  $\rho_P$  of 0.89 (90% confidence interval of 0.82–0.95), Gpat\_Acly with a  $\rho_A$  of 0.58 (90% confidence interval of 0.16–0.96), and GlIs with  $\rho_A$  of 0.46 (90% confidence interval of 0.14–0.96) (Figure 6A). Thus, we investigated phosphorylation that could regulate Glut4 (glucose uptake) and allosteric effectors that could regulate Gpat\_Acly (TG synthesis) or GlIs (glutaminase). For these reactions, we determined key regulatory molecules as the most robustly selected regulatory molecules for the estimation errors of metabolic fluxes (Transparent Methods).

The reaction mediated by Glut4 had 17 candidate regulatory molecules (17 phosphorylation sites of proteins of Glut4 and AS160) (Table S3). Among the candidate regulatory molecules of phosphorylation, phosphorylation of AS160 at S595 was determined as the key regulatory molecule of flux through Glut4 (Figures 6B and S5B). This result is consistent with earlier observations that the phosphorylation site S595 is located within a consensus phospho-Akt substrate motif (RXRXXS\*/T\*) (Treebak et al., 2010) and phosphorylation of AS160 in response to insulin results in Glut4 translocation via Rabs (Huang and Czech, 2007), indicating the validity of our kinetic trans-omic analysis.

The reaction mediated by Gpat\_Acly had 19 candidate regulatory molecules, including seven phosphorylation sites of proteins and 12 allosteric effectors, such as G6P, F6P, and F1,6BP, F2,6BP, and phosphoenolpyruvate. Among the candidate regulatory molecules, G6P or F6P was determined as the key regulatory molecule of flux through Gpat\_Acly (Figures 6B and S5B). This result is consistent with the earlier observations that both G6P and F6P are allosteric activators for Acly (Potapova et al., 2000), an important step in fatty acid synthesis (Song et al., 2018). Because G6P and F6P are highly correlated, it is difficult to distinguish the separate influence of these two allosteric effectors on Gpat\_Acly flux. Although phosphorylation of Acly by Akt has been shown to activate this reaction (Song et al., 2018), phosphorylation of Acly was not determined as the key regulatory molecule for Gpat\_Acly. The effect of phosphorylation of Acly did not meet the criteria of  $\rho_P$  above zero with a 90% confidence interval. This is possibly because of lack of phosphoproteomic data in the control condition, resulting in inaccurate prediction of the contribution of phosphorylation to Acly regulation. Addition of phosphoproteomic data in the Ctrl condition is needed to conclude whether phosphorylation of Acly is a key regulatory molecule in the glucose metabolism in insulin-stimulated adipocytes.

The reaction mediated by GlIs had 17 candidate regulatory molecules, including 17 allosteric effectors, such as glutamate, glutamine, ATP, and G6P. Among the candidate regulatory molecules, glutamate, the allosteric inhibitor of the reaction, was determined as the key regulatory molecule of flux through GlIs (Figures 6B and S5B).

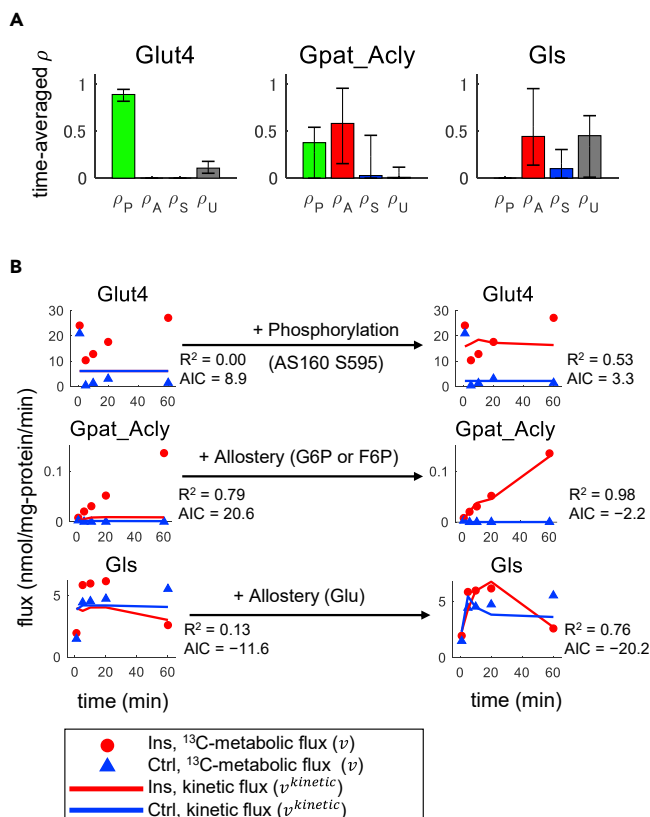


**Figure 6. Determination of Key Regulatory Molecules**

(A) Time-averaged regulation coefficients for reactions with 90% confidence intervals of  $\rho_P$  or  $\rho_A > \text{zero}$ . Error bars indicate the 90% confidence intervals. The confidence intervals were calculated from 200 sets of sampled parameters (see Transparent Methods).

(B) Effect of key regulatory molecules on kinetic flux models. The dots indicate estimated flux changes over time by metabolic flux analysis under non-steady-state conditions ( $v$ ), and the lines indicate kinetic fluxes ( $v^{kinetic}$ ) for the indicated metabolic enzymes. Kinetic fluxes with (right) or without (left) the indicated key regulatory molecules. Shown are the regulatory molecules that produced the smallest AIC when added to the model calculated with substrates and products.  $R^2$  and AIC values are indicated. A lower or more negative AIC value represents better fit. Note that kinetic fluxes through Glut4 without regulatory molecules in the Ins and Ctrl conditions are the same and the red and blue lines are overlapped. See also Figure S5A, Tables S3 and S4, and Data S1.

Thus, our kinetic trans-omic model predicted that insulin regulates flux changes through three key reactions. Phosphorylation of AS160 at S595 promoted flux through the Glut4 reaction to stimulate glucose uptake, allosteric activation of Acyl in Gpat\_Acyl by G6P or F6P stimulated TG synthesis, and alleviation of allosteric inhibition of GlS by glutamate stimulated glutamate synthesis (Figure 7).

## DISCUSSION

We developed a kinetic trans-omic analysis and identified key regulatory mechanisms, such as key regulatory events and molecules, controlling the activity of the proteins and enzymes mediating the reactions (Figure 7). The analysis relied on previously acquired metabolomic (Krycer et al., 2017; Quek et al., 2020) and phosphoproteomic data (Humphrey et al., 2013), as well as data acquired as part of this study. This study describes the methodologies and provides insights into how glucose metabolism is regulated by insulin. An advantage that this study has over previous trans-omic studies (Gerosa et al., 2015; Hackett et al., 2016; Kawata et al., 2018; Krycer et al., 2017; Yugi et al., 2014) is that we assessed non-steady-state flux to identify key regulatory mechanisms in metabolisms. Different flux values among time in both Ins and Ctrl conditions facilitate an accurate kinetic modeling in our kinetic trans-omic analysis. Moreover, by evaluating the regulation of metabolism by insulin in a dynamic state, this study represents a more physiologically relevant condition than studies of steady-state conditions.

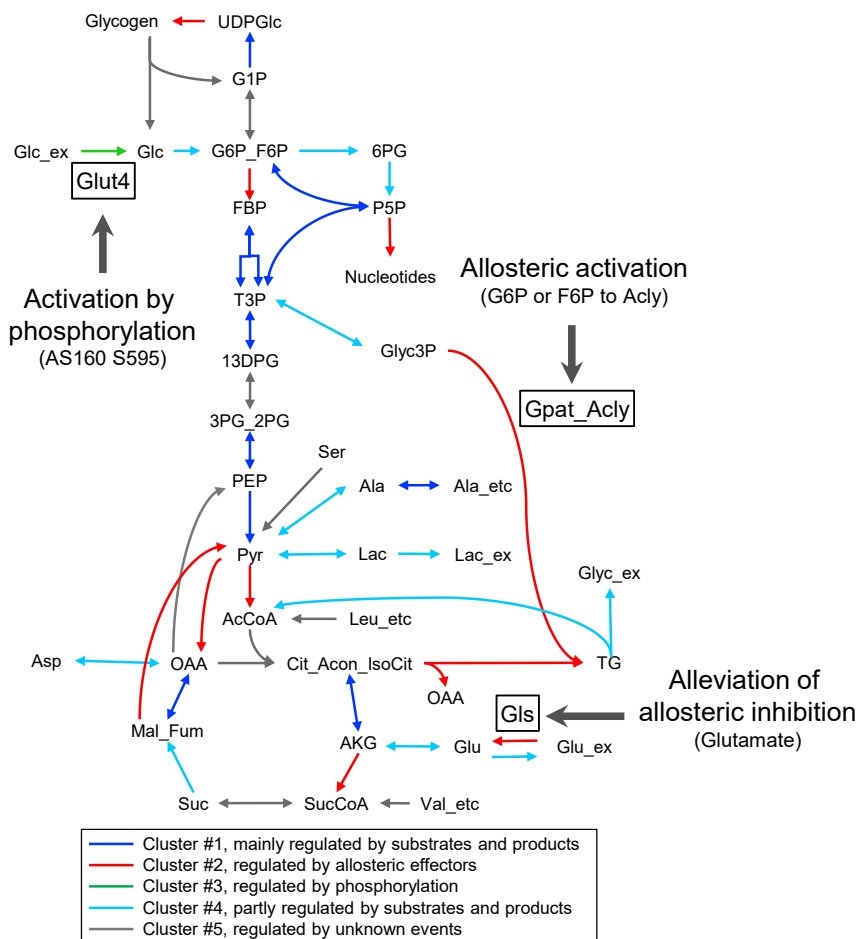


**Figure 7. Key Regulatory Mechanisms in the Glucose Metabolism in Insulin-Stimulated Adipocytes**

The colors of reactions correspond to the clusters in Figure 5B. Reactions in Figure 6 are emphasized by boxes and green and red bold arrows because the key regulatory molecules were selected for the reactions. In insulin-stimulated adipocytes, the reaction mediated by Glut4 is stimulated by phosphorylation of the protein AS160 at S595, the reaction mediated by Gpat\_Acly is stimulated by the allosteric effectors G6P or F6P, and the reaction mediated by Gls is stimulated by alleviating the allosteric effector glutamate.

Our kinetic trans-omic analysis revealed that three reactions—two controlled by allosteric effectors (reactions of Gpat\_Acly controlled by G6P or F6P and Gls controlled by glutamate) and one controlled by phosphorylation (the Glut4 reaction controlled by AS160)—were primary regulatory events in insulin-induced changes in metabolic flux of adipocytes. Except for the Glut4 reaction, which our model indicated was almost exclusively regulated by phosphorylation, our model indicates that most reactions were at least partially or predominantly controlled by amounts of substrates and products. Allosteric regulation strongly contributed to the flux through nine reactions, including those of Gpat\_Acly and Gls. Taken together, these findings indicated that insulin modulation of glycolytic flux in adipocytes is principally regulated by increased glucose uptake through Glut4, rather than by regulating the activity of glycolytic enzymes.

Previously, we described flux changes as B-spline functions (Quek et al., 2020); here, we used piecewise linear functions where the number of time intervals were different among reactions. The B-spline method is potentially able to represent more complex flux changes over time than the present method, whereas the present method can represent flux changes with smaller number of parameters than Quek et al.'s method. The present method would facilitate reduction in estimation errors by preventing overfitting. We compared the predicted fluxes using two methods (Figures S6 and S7) and identified high correlations (Pearson's correlation coefficient >0.6) for fluxes through glycolysis, including Glut4, glyceraldehyde -3-phosphate dehydrogenase (Gapd), phosphoglycerate kinase 1 (Pkg1), and enolase (Eno); through the oxidative PP pathway

including G6P dehydrogenase (G6pd) and 6-phosphogluconate dehydrogenase (Pgd); and through lactate dehydrogenase (Ldh) and the lactate transporter (Mct1), indicating that our model predicted the fluxes through these reactions with reasonable accuracy. These results indicate that fluxes calculated by each method are, in principle, consistent in glucose metabolism proximal to glucose uptake. A consistent difference between the two approaches was in the fluxes in the early time points in the Ctrl condition for which the B-spline method calculated fluxes larger than those calculated by the method using the piecewise linear function (Figures S6 and S7B). This would be because fluxes in the Ins and Ctrl conditions are independently calculated in the Quek et al.'s study, whereas fluxes at 0 min in both the Ins and Ctrl conditions were set at the same parameter values in the present study. As adipocytes were stimulated with insulin at 0 min, fluxes at 0 min in the Ins and Ctrl conditions should be the same values and the present study may provide physiologically more relevant fluxes in the early time points than the Quek et al.'s study.

Kinetic trans-omic analyses of metabolic flux under steady-state conditions have been reported. These studies included changes in gene expression (transcriptomic data) (Gerosa et al., 2015) or changes in protein abundance (proteomic data) (Hackett et al., 2016). These studies were of either *Escherichia coli* growing exponentially on eight different carbon sources (Gerosa et al., 2015) or yeast grown under 25 different chemostat conditions (Hackett et al., 2016). We did not consider changes in enzyme abundance (through altered gene expression or protein degradation) as a regulatory event of flux because we focused on an acute metabolic response to insulin in a short (60 min) timescale. Measuring protein abundance and incorporating such data into reaction kinetics would require analysis of a longer timescale.

According to another recent study (Tanner et al., 2018), reactions mediated by the glucose transporter (Glut1, Glut3, and Glut5), hexokinase (Hk2), phosphofructokinase (Pfk1), and the lactate transporter (Mct4) are rate limiting in a pathway from glucose uptake to lactate secretion in mammalian immortalized baby mouse kidney (iBMK) cells. In addition, overexpression of phosphofructo-2-kinase/fructose-2,6-bisphosphatases 1 and 3 (Pfkfb1 and Pfkfb3), which produces F2,6BP, activates flux in the pathway. In this study, we obtained similar results for the glucose transporter and hexokinase. The contribution of phosphorylation of AS160 to the flux differences between the Ins and Ctrl conditions (time-averaged  $\rho_P$ ) for Glut4 was 0.89 (Figure 6A), indicating that glucose uptake is the key reaction of glucose metabolism in insulin-stimulated adipocytes. In our model, Hk2 had a small contribution of substrates to the flux differences between the Ins and Ctrl conditions (time-averaged  $\rho_S$  of 0.12) (Figure S5A), indicating that the contribution of changes in substrate concentrations are small. Hk2 had a larger contribution from unknown regulators (time-averaged  $\rho_U$  of 0.88) (Figure S5A), indicating that the mechanism of insulin-dependent regulation remains to be determined. In contrast to Tanner et al. (2018), phosphofructokinase was not rate limiting in our model. We measured F1,6BP and F2,6BP separately by ion chromatography-MS (Hirayama et al., 2020) and found that the regulatory molecules for Pfk1 in insulin-stimulated adipocytes were the substrate F6P and allosteric effectors, including F6P and ADP (Figure S5A, Table S3). Measured F2,6BP amounts were similar between the Ins and Ctrl conditions (Figure S8), indicating that this potential allosteric effector did not regulate Pfk1 fluxes. Thus, comparison of our study and that of Tanner et al. (2018) indicated that key regulatory mechanisms of glycolytic flux depend on cell type and experimental conditions, and that multi-omic measurements from samples under the same experimental condition is necessary to identify key regulatory mechanisms.

Here, we classified reactions in glucose metabolism in adipocytes into five clusters using hierarchical clustering based on regulation coefficients, which represents contribution of regulatory events by enzyme phosphorylation, allosteric effectors, substrates, and products, to flux differences between the Ins and Ctrl conditions (Figure 5B). In Quek et al., 2020, we classified reactions into eight clusters using k-means clustering based on flux differences between the Ins and Ctrl conditions. In Krycer et al., 2017, we classified metabolites into five clusters using hierarchical clustering based on differences in metabolite concentrations between the Ins and Ctrl conditions. In all three studies, we found that reactions in the TCA cycle were classified into multiple clusters: four clusters in this study (Figures 5C and 7) and in Krycer et al. (2017) and three clusters in Quek et al. (2020). Thus, collectively these three studies indicated that the TCA cycle is regulated as functionally separate blocks, rather than as a single cycle, in the insulin-stimulated adipocytes.

In this study, flux estimation and identification of regulatory mechanisms of metabolism were sequentially performed. Flux estimation and identification of regulatory mechanisms can be performed in parallel by

developing a kinetic model of metabolism directly from multi-omic data, which requires explicit knowledge of regulatory mechanisms and simultaneous flux estimation and identification of regulatory mechanisms for all reactions, resulting in combinatorial explosion and large computational cost. By contrast, our method does not require explicit knowledge of regulatory molecules for flux and identification of the regulatory molecules can be performed for each reaction independently, because flux is already estimated before kinetic modeling. Thus, our sequential method has a lower computational cost. Furthermore, our method can be applied to any metabolic pathway and can predict the contribution of unknown regulators to flux, leading to new hypotheses about metabolic regulation.

In conclusion, we developed a kinetic trans-omic analysis using time-resolved  $^{13}\text{C}$ -glucose-labeled metabolomic and phosphoproteomic data from insulin-stimulated adipocytes and identified the enzyme phosphorylation and allosteric effectors with the greatest impact on glucose flux in response to insulin. Our approach can be widely applied to analyze the regulation in metabolism both *in vitro* and *in vivo*, and can provide new insights into metabolic diseases, such as type 2 diabetes.

### Limitation of the Study

Although we successfully quantitatively identified key regulatory events in insulin-stimulated adipocytes, there remain reactions with large  $\rho_U$  values (Cluster #5 in Figure 5B), wherein the mechanism for regulation of flux is mostly unknown. A reason for this cluster could be the relatively large estimation errors for the metabolic fluxes of these reactions. For example, to simplify the analysis we did not compartmentalize reactions into different subcellular regions, such as between the cytoplasm and mitochondria. This might cause inaccurate flux calculations, especially in the TCA cycle. We used  $[\text{U-}^{13}\text{C}]\text{glucose}$  as the source of the tracer, and alternate source of tracers, such as  $^{13}\text{C}$ -glutamine (Walther et al., 2012) and partially  $^{13}\text{C}$ -labeled glucose, in which only a part of the carbon atoms is  $^{13}\text{C}$ -labeled, could improve estimation precision of overall fluxes in glucose metabolism in mammal cells (Jang et al., 2018; Munger et al., 2008; Walther et al., 2012). Large estimation errors for the concentrations of metabolites lacking experimental measurements, such as pyruvate and oxaloacetate (Figure S2), could also cause large  $\rho_U$  values for reactions for which substrates, products, and allosteric effectors are such metabolites. Another possibility for the large  $\rho_U$  could be that main regulatory events of these reactions are not included in our candidate regulatory molecules (substrates, products, enzyme phosphorylation, and allosteric effectors).

### Resource Availability

#### Lead Contact

Further information and requests for resources and reagents should be directed to and will be fulfilled by the Lead Contact, Shinya Kuroda ([skuroda@bs.s.u-tokyo.ac.jp](mailto:skuroda@bs.s.u-tokyo.ac.jp)).

#### Materials Availability

This study did not generate new unique reagents. Metabolomic and phosphoproteomic data from insulin-stimulated 3T3-L1 adipocytes in our previous studies (Humphrey et al., 2013; Krycer et al., 2017; Quek et al., 2020) are used in this study.

#### Data and Code Availability

The datasets generated during this study are in the published article. The MATLAB code for  $^{13}\text{C}$ -metabolic flux analysis under non-steady-state conditions and kinetic modeling to identify key regulatory mechanisms are available at GitHub ([https://github.com/Satoshi-Ohno/Ohno\\_et\\_al\\_2020](https://github.com/Satoshi-Ohno/Ohno_et_al_2020)).

## METHODS

All methods can be found in the accompanying [Transparent Methods supplemental file](#).

## SUPPLEMENTAL INFORMATION

Supplemental Information can be found online at <https://doi.org/10.1016/j.isci.2020.101479>.

## ACKNOWLEDGMENTS

We are grateful to Dr. Shinsuke Uda, Dr. Hiroyuki Kubota, Dr. Fumio Matsuda, Dr. Hiroshi Shimizu, Dr. Yoshihiro Toya, and our laboratory members for fruitful discussion. We thank Nancy R. Gough, BioSerendipity,

LLC, for writing and editorial assistance. The computational analysis of this work was performed in part with support of the super computer system of National Institute of Genetics (NIG), Research Organization of Information and Systems (ROIS). This research was facilitated by access to Sydney Mass Spectrometry, a core research facility at the University of Sydney.

This work was supported by the Creation of Fundamental Technologies for Understanding and Control of Biosystem Dynamics, CREST (JPMJCR12W3) from the Japan Science and Technology Agency (JST), and by the Japan Society for the Promotion of Science (JSPS) KAKENHI Grant Number (17H06300, 17H06299, 18H03979). S.O. was funded by JSPS KAKENHI Grant Number JP17K14864. L.-E.Q. was funded by the Judith and David Coffey Fund, and Cancer Institute NSW. J.R.K. was funded by an NHMRC Early Career Fellowship (APP1072440), Australian Diabetes Society Skip Martin Early Career Fellowship, and Diabetes Australia Research grant. D.E.J. is an NHMRC Senior Principal Research Fellow (APP1019680). K.Y. was funded by JSPS KAKENHI Grant Number JP15H05582 and JP18H05431, and "Creation of Innovative Technology for Medical Applications Based on the Global Analyses and Regulation of Disease-Related Metabolites," PRESTO (JPMJPR1538) from JST. A.H. was funded by the Research on Development of New Drugs (GAPFREE) from the Japan Agency for Medical Research and Development, AMED. T.S. was funded by the AMED-CREST from AMED. A.H. and T.S. were funded from Yamagata prefectural government and the City of Tsuruoka.

## AUTHOR CONTRIBUTIONS

S.O., D.E.J., and S.K. conceived the project. S.O. performed the modeling. L.-E.Q., J.R.K., A.H., S.I., F.S., K.S., and T.S. performed experiments. S.O., L.-E.Q., K.Y., and J.R.K. analyzed the data. S.O. and S.K. wrote the manuscript. All authors read and approved the final manuscript.

## DECLARATION OF INTERESTS

The authors declare no competing interests.

Received: April 23, 2020

Revised: July 17, 2020

Accepted: August 17, 2020

Published: September 25, 2020

## REFERENCES

- Abate, A., Hillen, R.C., Aljoscha Wahl, S., and Wahl, S.A. (2012). Piecewise affine approximations of fluxes and enzyme kinetics from *in vivo* <sup>13</sup>C labeling experiments. *Int. J. Robust Nonlin. Control* 22, 1120–1139.
- Burnham, K.P., Anderson, D.R., and Huyvaert, K.P. (2011). AIC model selection and multimodel inference in behavioral ecology: Some background, observations, and comparisons. *Behav. Ecol. Sociobiol.* 65, 23–35.
- Cahill, G.F., Jeanrenaud, B., Leboeuf, B., and Renold, A.E. (1959). Effects of insulin on adipose tissue. *Ann. N. Y. Acad. Sci.* 82, 4303–4311.
- Cairns, R.A., Harris, I.S., and Mak, T.W. (2011). Regulation of cancer cell metabolism. *Nat. Rev. Cancer* 11, 85–95.
- Dimitriadis, G., Mitrou, P., Lambadiari, V., Maratou, E., and Raptis, S.A. (2011). Insulin effects in muscle and adipose tissue. *Diabetes Res. Clin. Pract.* 93, S52–S59.
- Gerosa, L., Haverkorn van Rijsewijk, B.R.B., Christodoulou, D., Kochanowski, K., Schmidt, T.S.B., Noor, E., and Sauer, U. (2015). Pseudo-transition analysis identifies the key regulators of dynamic metabolic Adaptations from steady-state data. *Cell Syst.* 1, 270–282.
- Giorgino, F., Laviola, L., and Eriksson, J.W. (2005). Regional differences of insulin action in adipose tissue: insights from *in vivo* and *in vitro* studies. *Acta Physiol. Scand.* 183, 13–30.
- Green, H., and Kehinde, O. (1975). An established preadipose cell line and its differentiation in culture II. Factors affecting the adipose conversion. *Cell* 5, 19–27.
- Hackett, S.R., Zanotelli, V.R.T., Xu, W., Goya, J., Park, J.O., Perlman, D.H., Gibney, P.A., Botstein, D., Storey, J.D., and Rabinowitz, J.D. (2016). Systems-level analysis of mechanisms regulating yeast metabolic flux. *Science* 354, aaf2786.
- Hirayama, A., Wakayama, M., and Soga, T. (2014). Metabolome analysis based on capillary electrophoresis-mass spectrometry. *Trends Anal. Chem.* 61, 215–222.
- Hirayama, A., Tabata, S., Kudo, R., Hasebe, M., Suzuki, K., Tomita, M., and Soga, T. (2020). The use of a double coaxial electrospray ionization sprayer improves the peak resolutions of anionic metabolites in capillary ion chromatography-mass spectrometry. *J. Chromatogr. A* 1619, 460914.
- Huang, S., and Czech, M.P. (2007). The GLUT4 glucose transporter. *Cell Metab.* 5, 237–252.
- Humphrey, S.J., Yang, G., Yang, P., Fazakerley, D.J., Stöckli, J., Yang, J.Y., and James, D.E. (2013). Dynamic adipocyte phosphoproteome reveals that Akt directly regulates mTORC2. *Cell Metab.* 17, 1009–1020.
- Humphrey, S.J., James, D.E., and Mann, M. (2015). Protein phosphorylation: a major switch mechanism for metabolic regulation. *Trends Endocrinol. Metab.* 26, 676–687.
- Israelsen, W.J., and Vander Heiden, M.G. (2015). Pyruvate kinase: function, regulation and role in cancer. *Semin. Cell Dev. Biol.* 43, 43–51.
- Jang, C., Chen, L., and Rabinowitz, J.D. (2018). Metabolomics and isotope tracing. *Cell* 173, 822–837.
- Jünger, M.A., and Aebersold, R. (2014). Mass spectrometry-driven phosphoproteomics: patterning the systems biology mosaic. *Wiley Interdiscip. Rev. Dev. Biol.* 3, 83–112.
- Katz, J., Landau, B.R., and Bartsch, G.E. (1966). The pentose cycle, triose phosphate isomerization, and lipogenesis in rat adipose tissue. *J. Biol. Chem.* 241, 727–740.
- Kawata, K., Hatano, A., Yugi, K., Kubota, H., Sano, T., Fujii, M., Tomizawa, Y., Kokaji, T., Tanaka, K.Y.,



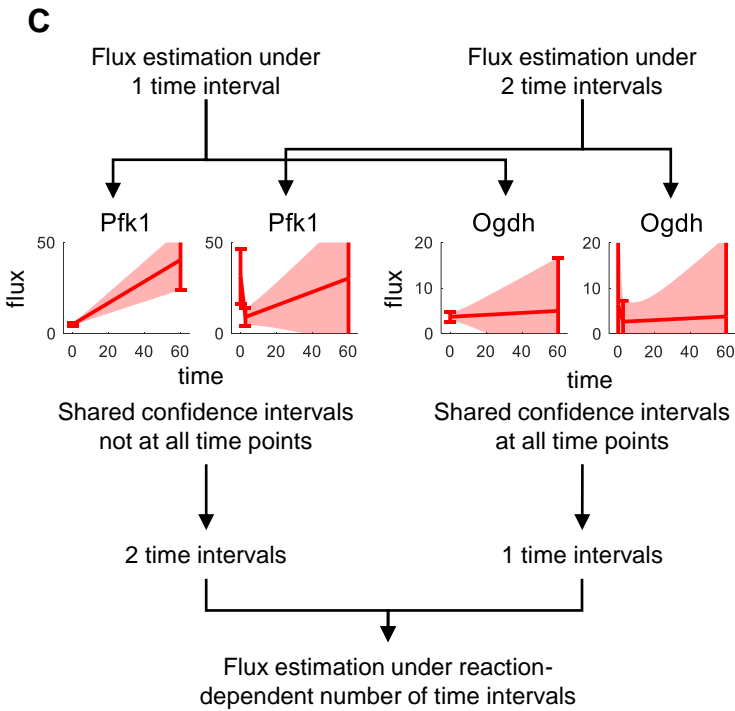
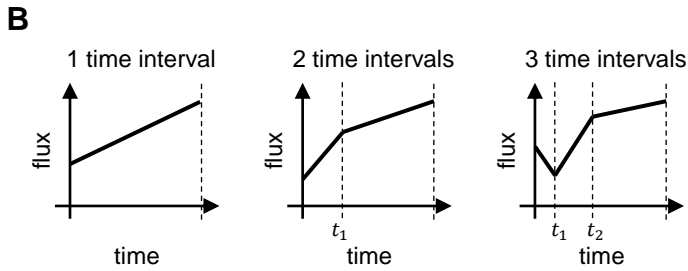
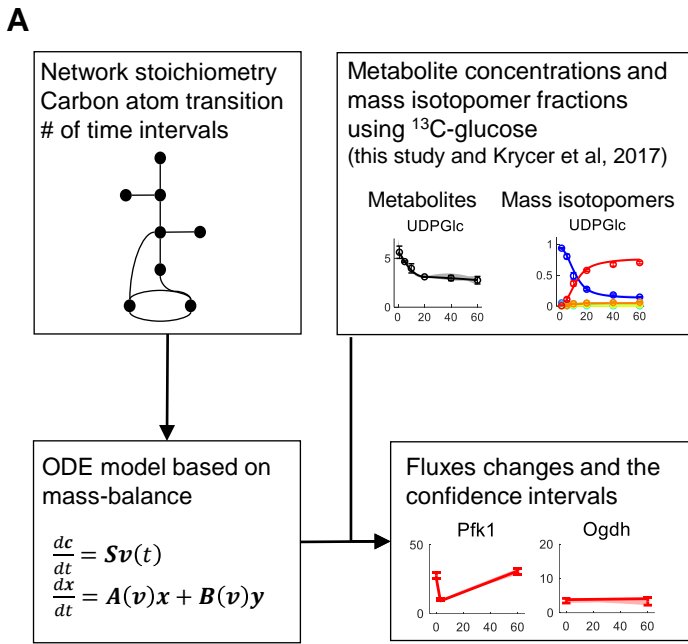
- Uda, S., et al. (2018). Trans-omic analysis reveals selective responses to induced and basal insulin across signaling, transcriptional, and metabolic networks. *iScience* 7, 212–229.
- Kochanowski, K., Sauer, U., and Noor, E. (2015). Posttranslational regulation of microbial metabolism. *Curr. Opin. Microbiol.* 27, 10–17.
- Krycer, J.R., Yugi, K., Hirayama, A., Fazakerley, D.J., Quek, L.-E., Scalzo, R., Ohno, S., Hodson, M.P., Ikeda, S., Shoji, F., et al. (2017). Dynamic metabolomics reveals that insulin primes the adipocyte for glucose metabolism. *Cell Rep.* 21, 3536–3547.
- Krycer, J.R., Elkington, S.D., Diaz-Vegas, A., Cooke, K.C., Burchfield, J.G., Fisher-Wellman, K.H., Cooney, G.J., Fazakerley, D.J., and James, D.E. (2020a). Mitochondrial oxidants, but not respiration, are sensitive to glucose in adipocytes. *J. Biol. Chem.* 295, 99–110.
- Krycer, J.R., Quek, L.E., Francis, D., Fazakerley, D.J., Elkington, S.D., Diaz-Vegas, A., Cooke, K.C., Weiss, F.C., Duan, X., Kurdyukov, S., et al. (2020b). Lactate production is a prioritized feature of adipocyte metabolism. *J. Biol. Chem.* 295, 83–98.
- Leighty, R.W., and Antoniewicz, M.R. (2011). Dynamic metabolic flux analysis (DMFA): a framework for determining fluxes at metabolic non-steady state. *Metab. Eng.* 13, 745–755.
- Liebermeister, W., Uhlenendorf, J., and Klipp, E. (2010). Modular rate laws for enzymatic reactions: thermodynamics, elasticities and implementation. *Bioinformatics* 26, 1528–1534.
- Liu, L., Shah, S., Fan, J., Park, J.O., Wellen, K.E., and Rabinowitz, J.D. (2016). Malic enzyme tracers reveal hypoxia-induced switch in adipocyte NADPH pathway usage. *Nat. Chem. Biol.* 12, 345–352.
- Macek, B., Mann, M., and Olsen, J.V. (2009). Global and site-specific quantitative phosphoproteomics: principles and Applications. *Annu. Rev. Pharmacol. Toxicol.* 49, 199–221.
- Mor, I., Cheung, E.C., and Voudsen, K.H. (2011). Control of glycolysis through regulation of PFK1: old friends and recent additions. *Cold Spring Harb. Symp. Quant. Biol.* 76, 211–216.
- Munday, K.A., Giles, I.G., and Poat, P.C. (1980). Review of the comparative biochemistry of pyruvate kinase. *Comp. Biochem. Physiol.* 67, 403–411.
- Munger, J., Bennett, B.D., Parikh, A., Feng, X.-J.J., McArdle, J., Rabinowitz, H.A., Shenk, T., and Rabinowitz, J.D. (2008). Systems-level metabolic flux profiling identifies fatty acid synthesis as a target for antiviral therapy. *Nat. Biotechnol.* 26, 1179–1186.
- Passonneau, J.V., and Lowry, O.H. (1963). P-Fructokinase and the control of the citric acid cycle. *Biochem. Biophys. Res. Commun.* 13, 372–379.
- Peng, B., Li, H., and Peng, X.-X. (2015). Functional metabolomics: from biomarker discovery to metabolome reprogramming. *Protein Cell* 6, 628–637.
- Placzek, S., Schomburg, I., Chang, A., Jeske, L., Ulbrich, M., Tillack, J., and Schomburg, D. (2017). BRENDA in 2017: new perspectives and new tools in BRENDA. *Nucleic Acids Res.* 45, D380–D388.
- Plum, L., Belgardt, B.F., and Brüning, J.C. (2006). Central insulin action in energy and glucose homeostasis. *J. Clin. Invest.* 116, 1761–1766.
- Potapova, I.A., El-Maghrabi, M.R., Doronin, S.V., and Benjamin, W.B. (2000). Phosphorylation of recombinant human ATP:citrate lyase by cAMP-dependent protein kinase abolishes homotropic allosteric regulation of the enzyme by citrate and increases the enzyme activity. Allosteric activation of atp:citrate lyase by phosphorylated sug. *Biochemistry* 39, 1169–1179.
- Quek, L.-E., Krycer, J.R., Ohno, S., Yugi, K., Fazakerley, D.J., Scalzo, R., Elkington, S.D., Dai, Z., Hirayama, A., Ikeda, S., et al. (2020). Dynamic <sup>13</sup>C flux analysis captures the reorganization of adipocyte glucose metabolism in response to insulin. *iScience* 23, 100855.
- Ray, P.D., Huang, B.-W., and Tsuji, Y. (2012). Reactive oxygen species (ROS) homeostasis and redox regulation in cellular signaling. *Cell Signal.* 24, 981–990.
- Salih, D.A., and Brunet, A. (2008). FoxO transcription factors in the maintenance of cellular homeostasis during aging. *Curr. Opin. Cell Biol.* 20, 126–136.
- Saltiel, A.R., and Kahn, C.R. (2001). Insulin signalling and the regulation of glucose and lipid metabolism. *Nature* 414, 799–806.
- Sandoval, P.C., Slentz, D.H., Pisitkun, T., Saeed, F., Hoffert, J.D., and Knepper, M.A. (2013). Proteome-wide measurement of protein half-lives and translation rates in vasopressin-sensitive collecting duct cells. *J. Am. Soc. Nephrol.* 24, 1793–1805.
- Schöneberg, T., Kloos, M., Brüser, A., Kirchberger, J., and Sträter, N. (2013). Structure and allosteric regulation of eukaryotic 6-phosphofructokinases. *Biol. Chem.* 394, 977–993.
- Song, Z., Xiaoli, A.M., and Yang, F. (2018). Regulation and metabolic significance of De Novo lipogenesis in adipose tissues. *Nutrients* 10, 1–22.
- Tanner, L.B., Goglia, A.G., Wei, M.H., Sehgal, T., Parsons, L.R., Park, J.O., White, E., Toettcher, J.E., and Rabinowitz, J.D. (2018). Four key steps control glycolytic flux in mammalian cells. *Cell Syst.* 7, 49–62.
- Treebak, J.T., Taylor, E.B., Witczak, C.A., An, D., Toyoda, T., Koh, H.-J., Xie, J., Feener, E.P., Wojtaszewski, J.F.P., Hirshman, M.F., et al. (2010). Identification of a novel phosphorylation site on TBC1D4 regulated by AMP-activated protein kinase in skeletal muscle. *Am. J. Physiol.* 298, C377–C385.
- Walther, J.L., Metallo, C.M., Zhang, J., and Stephanopoulos, G. (2012). Optimization of <sup>13</sup>C isotopic tracers for metabolic flux analysis in mammalian cells. *Metab. Eng.* 14, 162–171.
- Yamashita, T., Yamashita, K., and Kamimura, R. (2007). A stepwise AIC method for variable selection in linear regression. *Commun. Stat. Theory Methods* 36, 2395–2403.
- Yugi, K., and Kuroda, S. (2017). Metabolism as a signal generator across trans-omic networks at distinct time scales. *Curr. Opin. Syst. Biol.* 8, 59–66.
- Yugi, K., Kubota, H., Toyoshima, Y., Noguchi, R., Kawata, K., Komori, Y., Uda, S., Kunida, K., Tomizawa, Y., Funato, Y., et al. (2014). Reconstruction of insulin signal flow from phosphoproteome and metabolome data. *Cell Rep.* 8, 1171–1183.
- Yugi, K., Kubota, H., Hatano, A., and Kuroda, S. (2016). Trans-Omics: how to reconstruct biochemical networks across multiple “omic” layers. *Trends Biotechnol.* 34, 276–290.
- Yugi, K., Ohno, S., Krycer, J.R., James, D.E., and Kuroda, S. (2019). Rate-oriented trans-omics: integration of multiple omic data on the basis of reaction kinetics. *Curr. Opin. Syst. Biol.* 15, 109–120.
- Zamboni, N., Saghatelian, A., and Patti, G.J. (2015). Defining the metabolome: size, flux, and regulation. *Mol. Cell* 58, 699–706.

iScience, Volume 23

## **Supplemental Information**

### **Kinetic Trans-omic Analysis Reveals Key Regulatory Mechanisms for Insulin-Regulated Glucose Metabolism in Adipocytes**

**Satoshi Ohno, Lake-Ee Quek, James R. Krycer, Katsuyuki Yugi, Akiyoshi Hirayama, Satsuki Ikeda, Futaba Shoji, Kumi Suzuki, Tomoyoshi Soga, David E. James, and Shinya Kuroda**



**D**

# of time intervals	z-score to determine # of time intervals	# of parameters	RSS	AIC
1	-	212	4991	2112
2	-	335	2199	1415
3	-	458	1906	1497
	4.00	231	3929	1875
	3.00	249	3325	1719
	2.00	266	2857	1579
	1.50	273	2693	1525
reaction dependent	1.00	281	2678	1534
	0.75	294	2546	1502
	0.60	315	2242	1397
	0.50	329	2212	1410
	0.40	346	2128	1400
	0.30	377	2081	1436

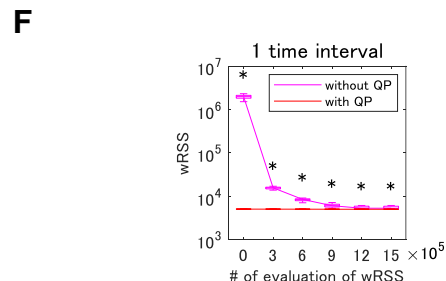
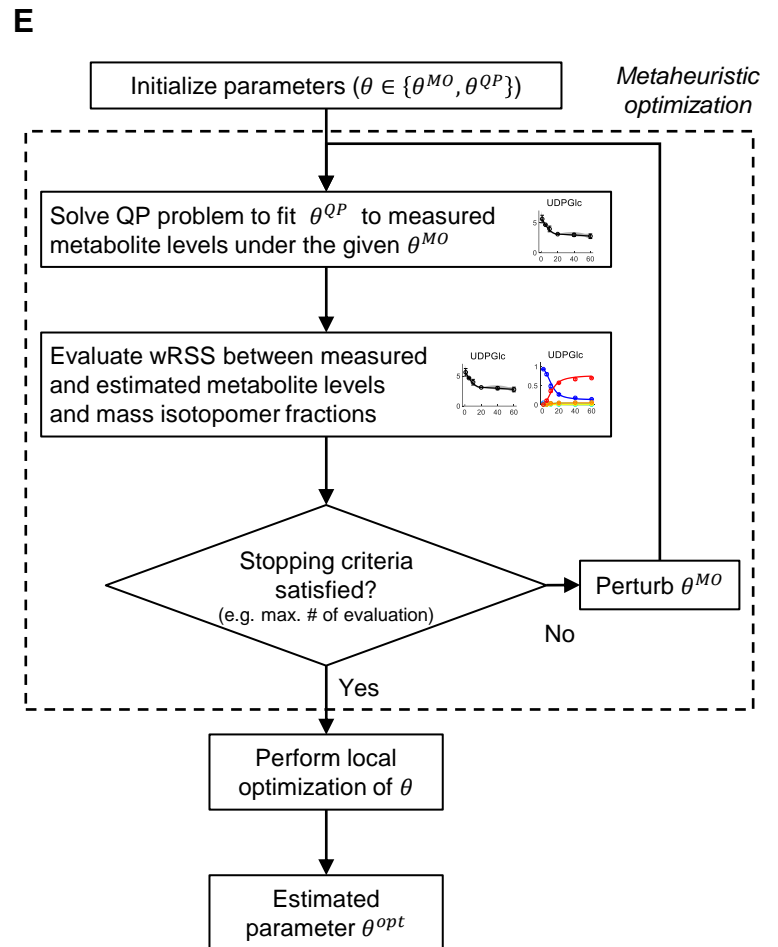


**Figure S1. Procedures of estimation of flux changes under non-steady-state conditions. Related to Figures 2 and 3.**

(A) Overview of estimation of flux changes under non-steady-state conditions.

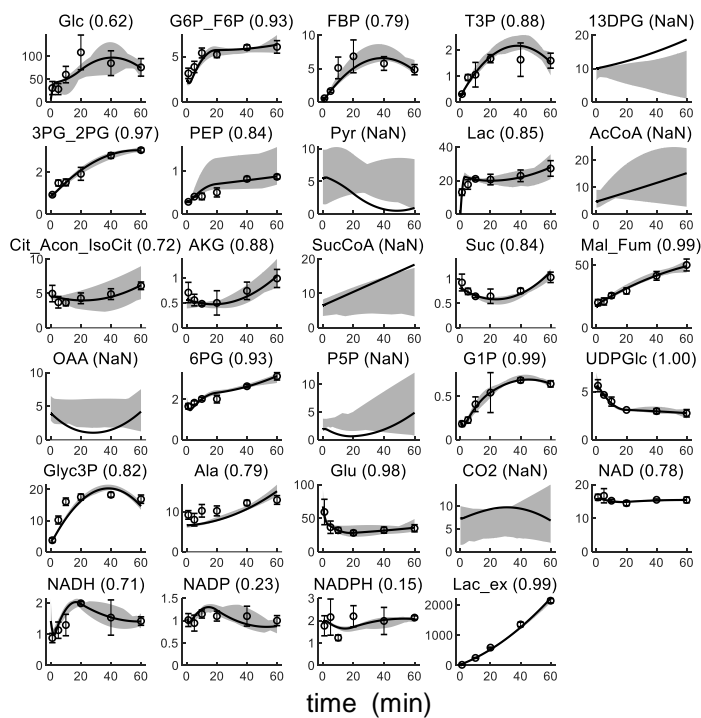
(B) Flux described as a piecewise linear function in the time domain with switch times (times when the slope of flux changes). The switch times are represented as  $t_1$  under 2 time intervals, and as  $t_1$  and  $t_2$  under 3 time intervals.

(C) Determination of reaction-dependent number of time intervals (see Transparent Methods).

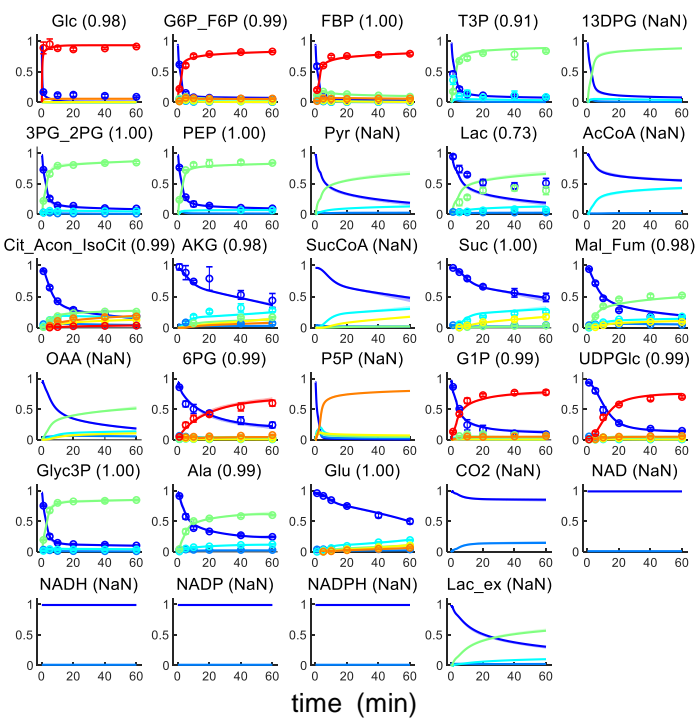
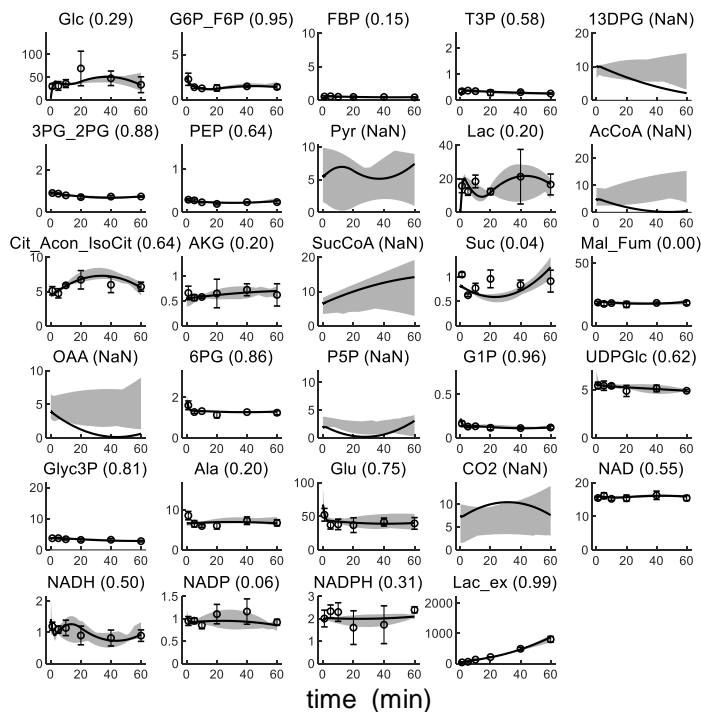
(D) AIC of the models with the same number of time intervals among all reactions and the model with reaction-dependent number of time intervals. AIC is defined as  $N \log(\text{wRSS}/N) + 2p$ , where  $N$  is the number of residuals and  $p$  is the number of parameters.

(E) Optimization procedure of parameters using quadratic programming (QP) (see Transparent Methods).

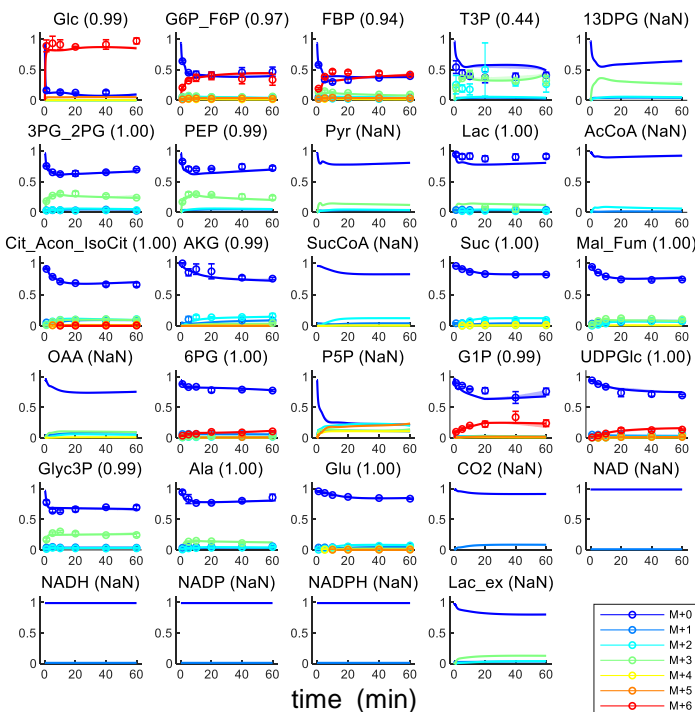
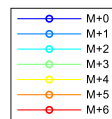
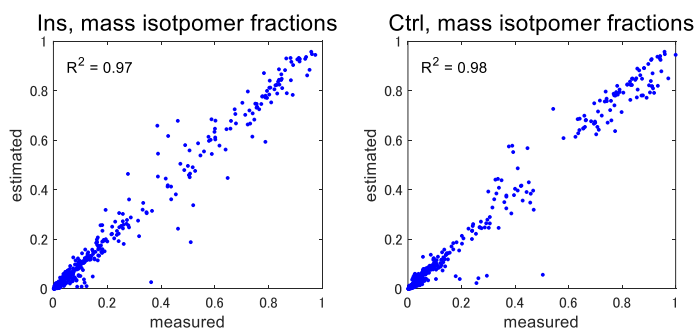
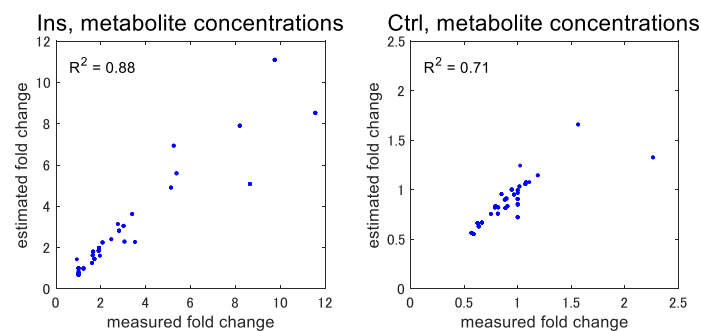
(F) Convergence profiles of metaheuristic optimization with or without use of QP under one time interval. The same number of time intervals was set among all reactions. The lines connect the median values among 30 independent optimizations. The box encompasses the 25th to 75th percentiles, and the whiskers indicate the maximum and minimum values. The medians of the wRSS were compared between optimizations with and without use of QP using Wilcoxon rank-sum test with the Bonferroni multiple testing correction. P values < 0.01 were considered statistically significant and are indicated with an asterisk (\*). Metaheuristic optimization without use of QP under two and three time intervals was not able to be performed under our optimization condition because initial parameters in the optimization were not updated even after one week.

**A****Ins** Metabolite concentrations (nmol/mg-protein)

## Mass isotopomer fractions

**Ctrl** Metabolite concentrations (nmol/mg-protein)

## Mass isotopomer fractions

**B**

**Figure S2. All measured and estimated metabolite concentrations and mass isotopomer fractions. Related to Figure 2.**

(A) All measured and estimated metabolite concentrations and mass isotopomer fractions. The circles and the error bars indicate the mean and the standard deviations of the measurements from 3 separate experiments (Krycer et al., 2017). The lines and the shaded areas indicate optimal estimates with the 90% confidence intervals. M+*i* indicates mass isotopomer with *i* carbons labelled with <sup>13</sup>C. The numbers next to the metabolite names indicates R<sup>2</sup> values between measured and estimated concentrations or mass isotopomer fractions. Note that media were exchanged at 0 min in both the conditions. The optimal estimates can be outside the confidence intervals due to sampling from a truncated multivariate normal distribution and the curse of dimensionality (Verleysen and François, 2005). Abbreviations of metabolites are defined in Table S1, and the data of estimated concentrations are shown in Table S2.

(B) Scatter plots of all measured and estimated metabolite concentrations and mass isotopomer fractions. Measured and estimated metabolite concentrations are shown as fold changes to measured concentrations at 1 min.

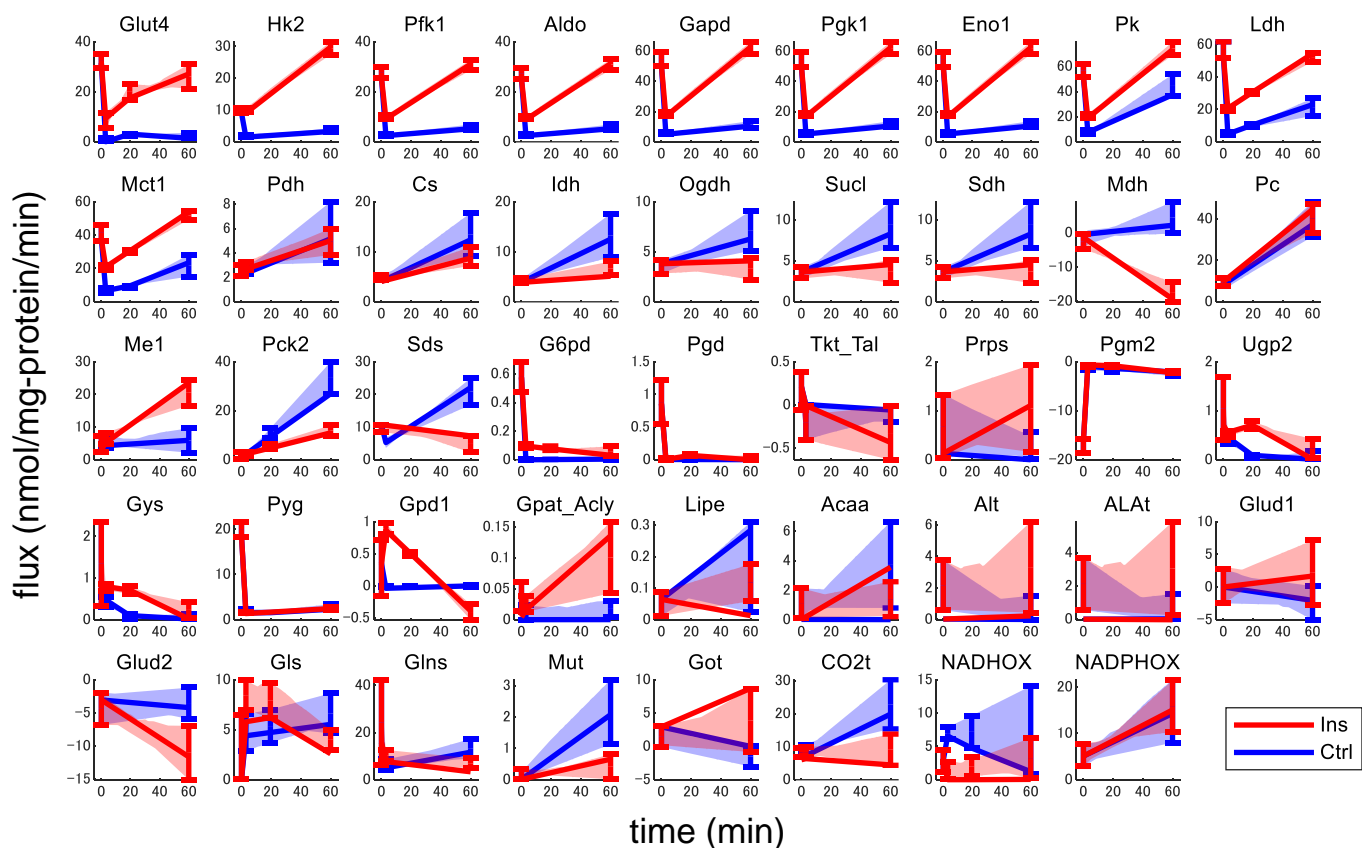
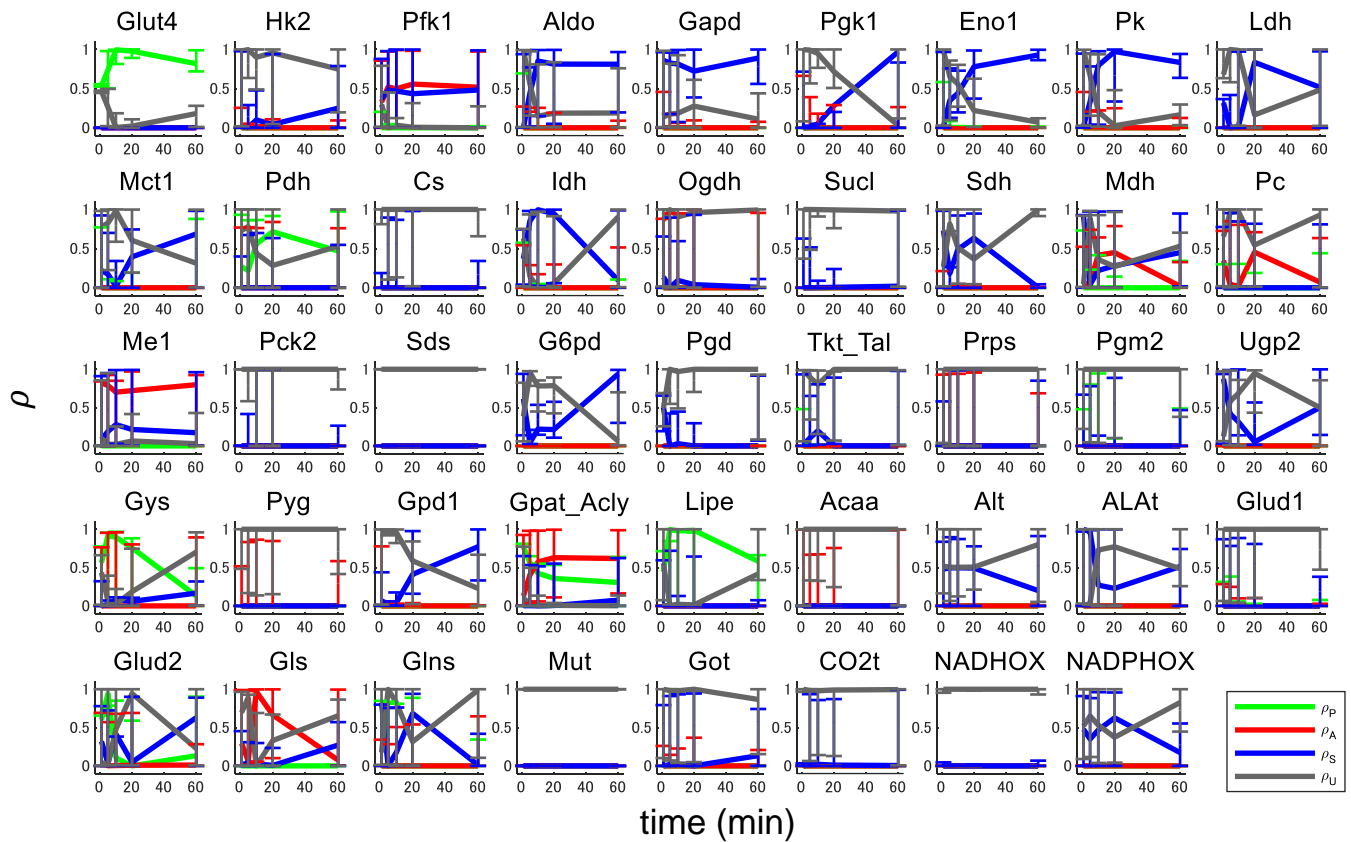


**Figure S3. All estimated flux changes. Related to Figure 3.**

The lines and the shaded areas indicate optimal estimates (Table S2) with the 90% confidence intervals. Error bars indicate the 90% confidence intervals at switch times (times when the slope of flux changes), as well as 0 and 60 min. Number of time intervals (and switch times) were set among reactions (see Transparent Methods). The confidence intervals were calculated from 200 sets of sampled parameters under constraints based on the covariance matrix of the estimated parameters (see Transparent Methods). Note that the optimal estimates can be outside the confidence intervals due to sampling from a truncated multivariate normal distribution and the curse of dimensionality (Verleysen and François, 2005). Abbreviations of reactions are defined in Table S1, and the data of estimated fluxes are shown in Table S2.

**A**



**B**

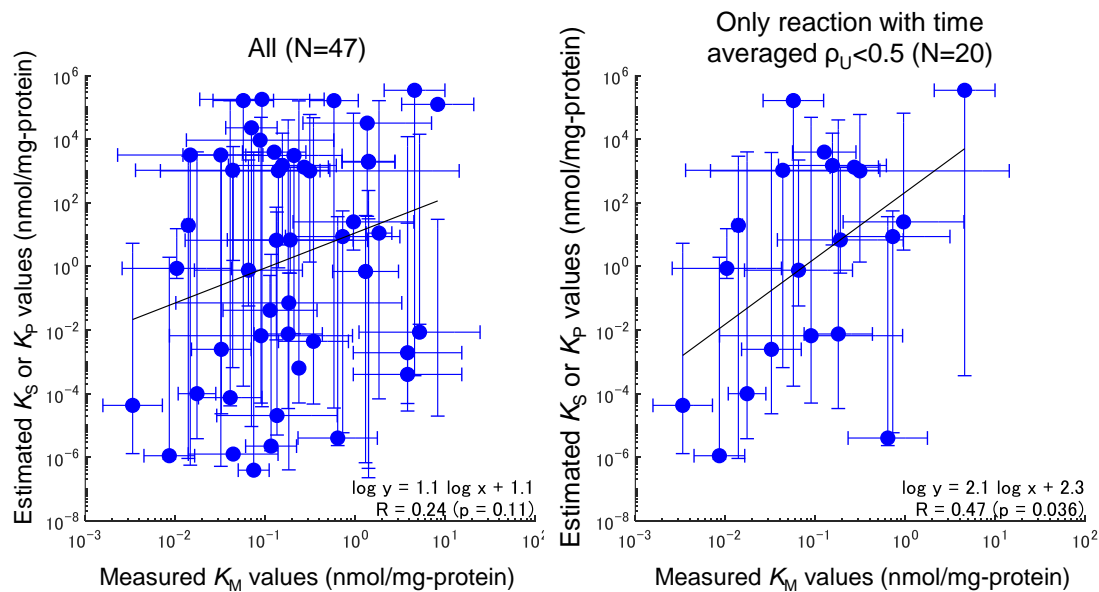


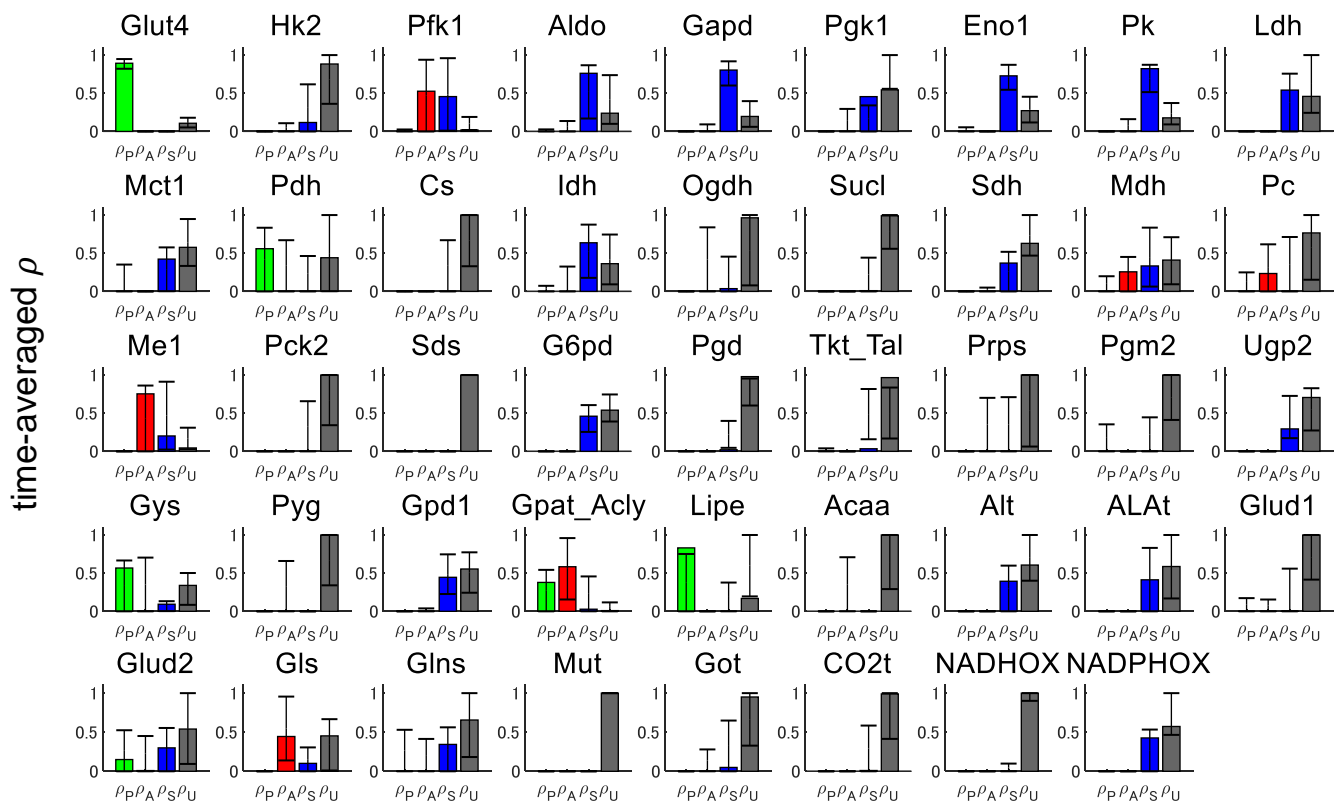
**Figure S4. Time courses of regulation coefficients and comparison of Michaelis-Menten constants estimated in this study with those experimentally measured. Related to Figure 5.**

(A) Time courses of regulation coefficients of enzyme phosphorylation ( $\rho_P$ ), allosteric effectors ( $\rho_A$ ), substrates and products ( $\rho_S$ ), and unaccounted regulators ( $\rho_U$ ). The regulation coefficients were calculated at 1, 5, 10, 20, and 60 min. The lines indicate regulation coefficients calculated from optimal estimates of parameters in our metabolic flux analysis. Error bars indicate the 90% confidence intervals. The confidence intervals were calculated from 200 sets of sampled parameters (see Transparent Methods). Abbreviations of reactions are defined in Table S1.

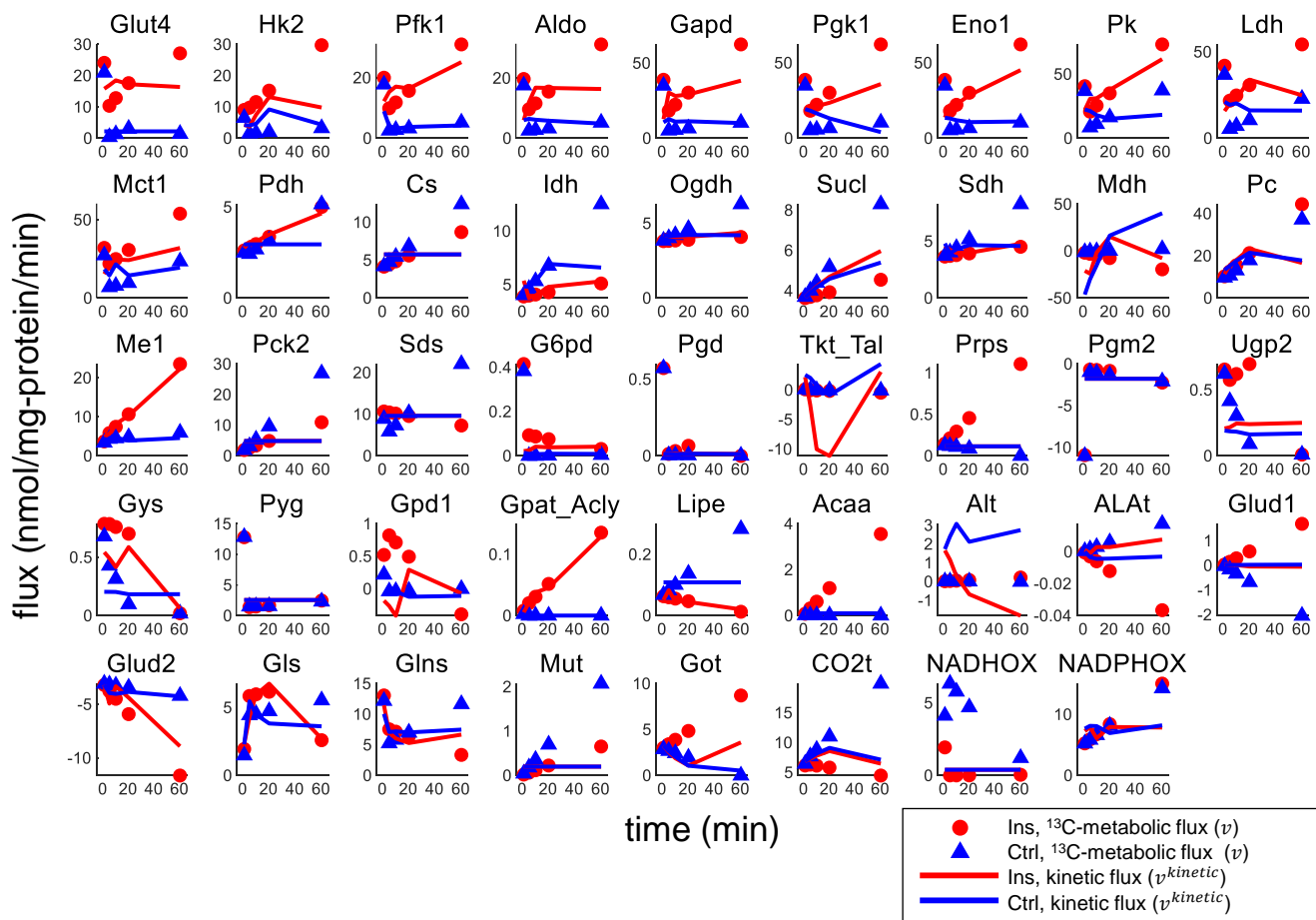
(B) Comparison of Michaelis-Menten constants estimated in this study with those reported in the BRENDA database for all reaction (left) and for only reaction with the time averaged  $\rho_U$  smaller than 0.5 (right). The dots represent the geometric mean of the measured  $K_M$  values versus estimated  $K_S$  or  $K_P$  values using optimal flux estimates in the metabolic flux analysis. The error bars of measured values represent the geometric standard deviations and the error bars of estimated values represent 90% confidence intervals, calculated from 200 sets of sampled parameters. N represents the number of dots. The regression lines of the dots, Pearson's correlation coefficients (R), and the p-values are shown.



**A**



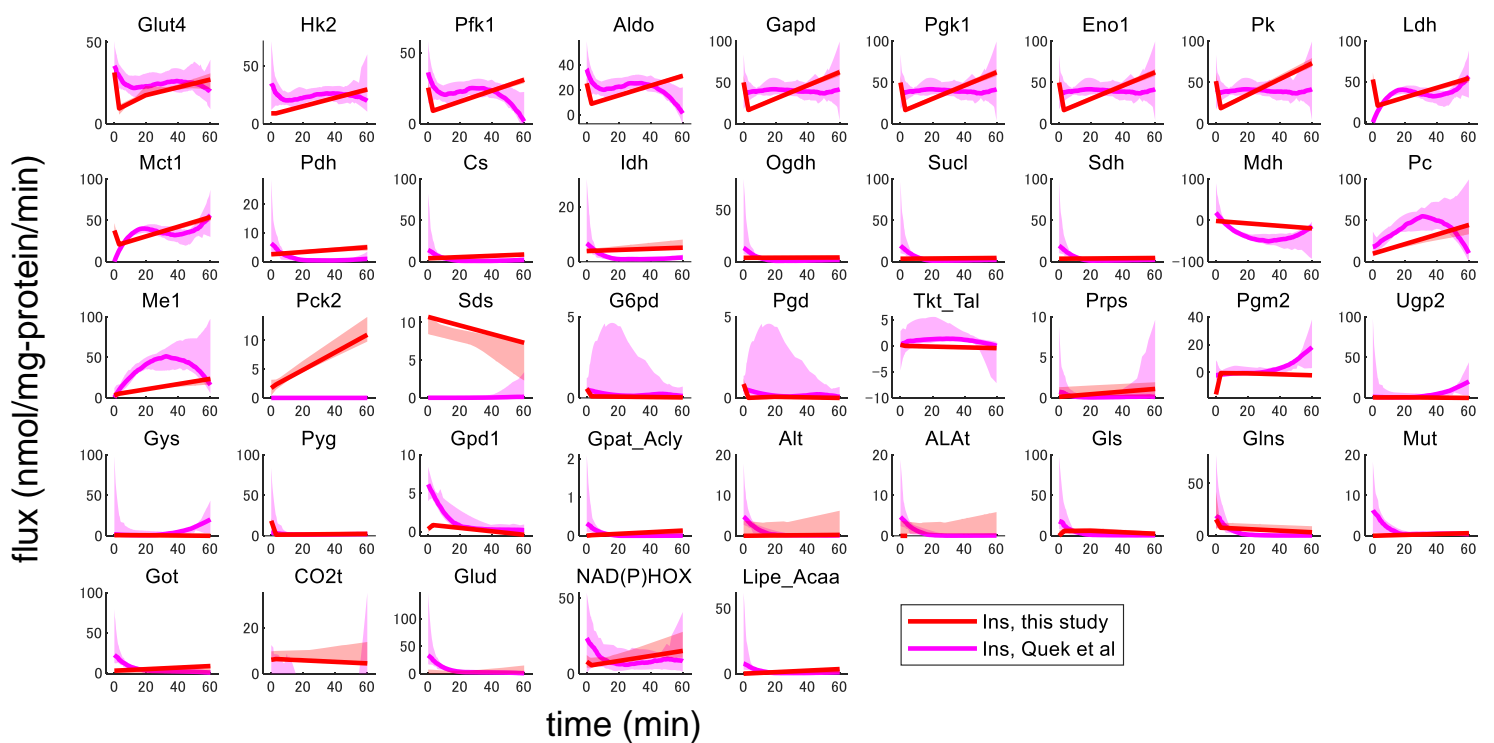
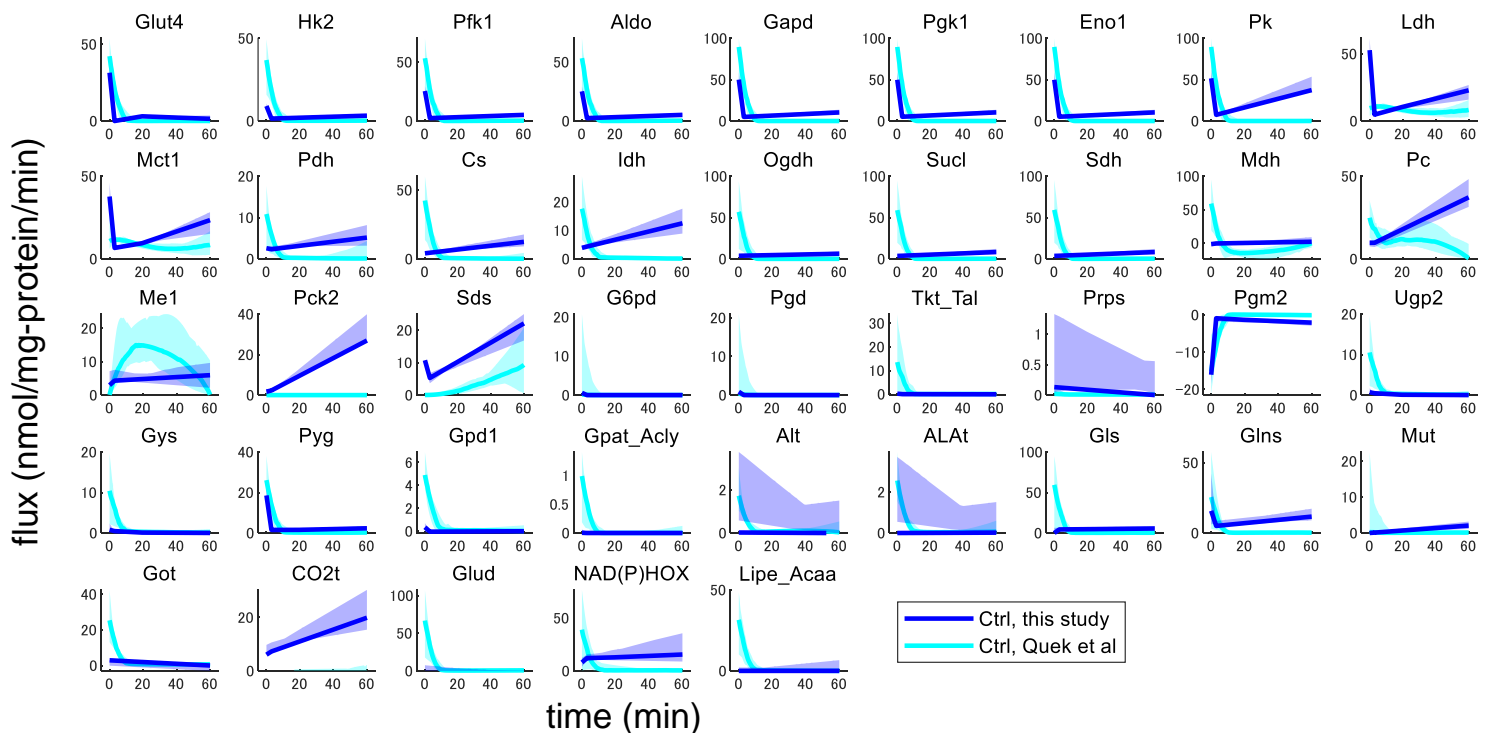
**B**



**Figure S5. Time-averaged regulation coefficients and comparison of  $^{13}\text{C}$ -metabolic fluxes with kinetic fluxes for all reactions. Related to Figure 6.**

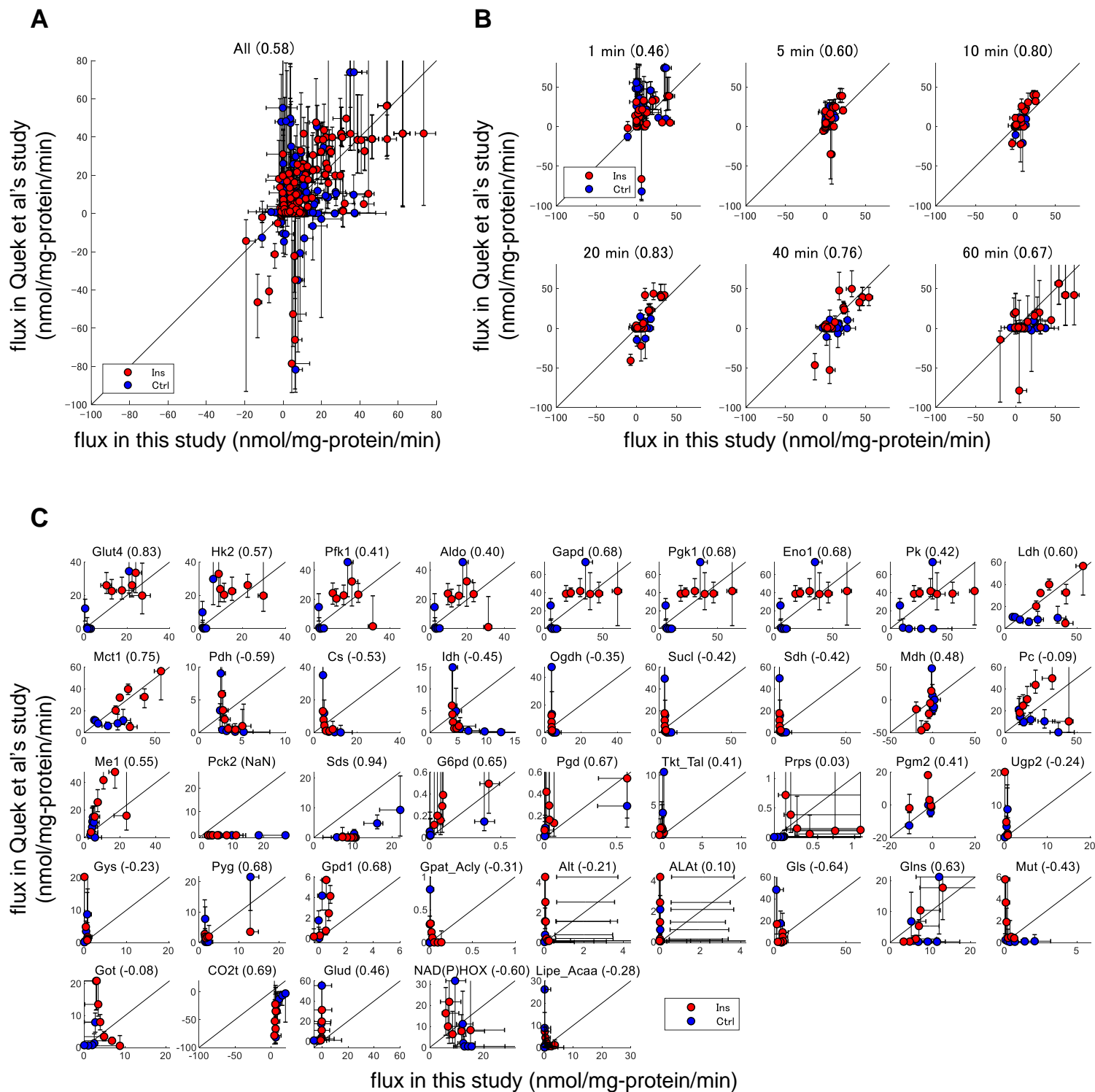
(A) Time-averaged regulation coefficients of enzyme phosphorylation ( $\rho_p$ ), allosteric effectors ( $\rho_A$ ), substrates and products ( $\rho_S$ ), and unaccounted regulators ( $\rho_U$ ). Error bars indicate the 90% confidence intervals. The confidence intervals were calculated from 200 sets of sampled parameters (see Transparent Methods). Note that the optimal estimates can be outside the confidence intervals due to sampling from a truncated multivariate normal distribution and the curse of dimensionality (Verleysen and François, 2005).

(B) Comparison of  $^{13}\text{C}$ -metabolic fluxes ( $v$ ), estimated by metabolic flux analysis under non-steady state conditions, with kinetic fluxes ( $v^{\text{kinetic}}$ ) for all reactions. Abbreviations of reactions are defined in Table S1.

**A****B**

**Figure S6. Comparison of fluxes between this study and Quiek et al, 2020. Related to Figure 3.**

(A-B) All of estimated flux changes in this study and Quiek et al, 2020 in the Ins (A) and Ctrl (B) conditions. In this study, the optimal estimates and the 90% confidence intervals are shown. In Quiek et al., the median values of fluxes among Monte-Carlo sampling and the 90% confidence intervals are shown. Abbreviations of reactions are defined in Data S1F.



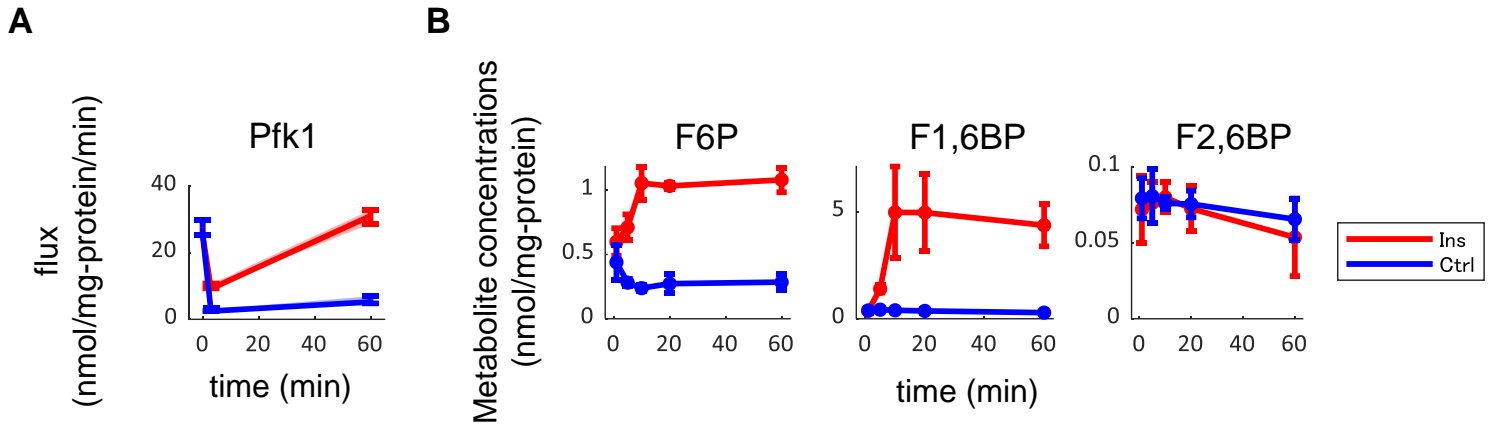


**Figure S8. The estimated flux through Pfk1 and the measured amounts of F6P, F1,6BP and F2,6BP. Related to Figure 5.**

(A) The estimated flux through Pfk1, same as in Figures 3B and S3.

(B) The measured amounts of F6P, F1,6BP and F2,6BP. The circles and the error bars indicate the mean and the standard deviations of the measurements from 3 separate experiments.

## TRANSPARENT METHODS

### <sup>13</sup>C-metabolic flux analysis under non-steady-state conditions

#### Metabolic network model

A metabolic network model was constructed for metabolic flux analysis under non-steady-state conditions (Figures 3A and Table S1). The model consists of 26 internal metabolites and 41 reactions (Table S1) and includes reactions of glycolysis, TCA cycle, PP pathway, anaplerotic reactions, glycogen synthesis and degradation, and TG synthesis and degradation. Although glucose production in adipocytes has not been reported (Cherrington, 1999), Pck2 was included in the model because Pck2 protein was expressed in adipocytes in our previous study (Humphrey et al., 2013).

Because G6P and F6P are adjacent and their isotopic ratios were similar, these metabolites were considered to be in rapid equilibrium and were summed as one metabolite, G6P\_F6P for simplicity (Figure 3A, Table S1). Similar to G6P and F6P, malate and fumarate were summed as one metabolite, Mal\_Fum, and citrate, aconitate, and isocitrate were summed as one metabolite as Cit\_Acon\_Icit. Also, 3-phosphogluconate and 2-phosphogluconate, and F1,6BP and F2,6BP were summed as one metabolite, 3PG\_2PG and FBP, respectively, because these metabolites were not separated by capillary electrophoresis-mass spectrometry (CE-MS) under our experimental conditions (Krycer et al., 2017). It should be noted that F1,6BP and F2,6BP were separated by ion chromatography-mass spectrometry (IC-MS) as described later, but we used the summed FBP in the metabolic network for metabolic flux analysis to use intracellular metabolome data obtained under the same measurement condition.

In the PP pathway, ribose 5-phosphate, ribulose 5-phosphate, and xylulose 5-phosphate were summed as one metabolite as P5P because ribulose 5-phosphate and xylulose 5-phosphate were not measured in our previous study (Krycer et al., 2017). To simplify the network model, erythrose 4-phosphate (E4P) and sedoheptulose 7-phosphate (S7P) were omitted in the PP pathway, and reactions associated with E4P and S7P were merged as one reaction (Table S1).

In TG synthesis, one molecule of TG is synthesized from one molecule of glycerol 3-phosphate and three molecules of fatty acids through the Gpat reaction. Fatty acids are synthesized from citrate through a series of reactions, for which Acly reaction is the first and important step in fatty acid synthesis (Potapova et al., 2000). We assumed that adipocytes in this study have the same fatty acid composition of TG as adipocytes of rats in a previous study (Body, 1988), leading to average 17.1 carbon atoms in fatty acids in TG. Therefore, we defined TG synthesis reaction in the model as Gpat\_Acly, where one molecule of TG is synthesised from one molecule of glycerol 3-

phosphate and 25.7 molecules of citrate. We did not include lipids other than TG in the model, because TG represents 90% of lipids in adipose tissue of animals (Body, 1988). Similar to TG synthesis, we described a reaction of TG degradation in which 25.8 molecules of acetyl-CoA are synthesized from one molecule of TG. ATP is not included in the model, because there are various reactions that consume ATP and including ATP would not affect overall fluxes in glucose metabolism. Compartmentation of reactions into cytoplasm and mitochondria was not considered and estimated fluxes using this model represents averaged fluxes, assuming a whole cell as a single compartment.

#### Flux change as a piecewise linear function of time

To model flux changes (Figures 2, 3 and Figures S1, S2, S3), we needed to describe flux changes as a function of time. Similar to previous studies (Abate et al., 2012; Leighty and Antoniewicz, 2011), flux changes were defined as a continuous piecewise linear function in the time domain with switch times ( $t_1, t_2, \dots, t_K$ ) between  $t_0$  (0 min) and  $t_{K+1}$  (60 min) (Figure S1B). Flux changes in a time interval between  $t_k$  and  $t_{k+1}$  were described by

$$\mathbf{v}(t) = \mathbf{v}_k + \frac{\mathbf{v}_{k+1} - \mathbf{v}_k}{t_{k+1} - t_k} (t - t_k), \quad t_k \leq t \leq t_{k+1}, \quad (1)$$

where  $\mathbf{v}$  is a vector of flux changes, and  $\mathbf{v}_k$  is a vector of fluxes at  $t_k$ . All functions for flux changes have the same switch times. Reversible reactions were modelled as separate forward and backward fluxes.

#### Equations for describing changes of metabolite concentrations over time under non-steady-state conditions

The mass balance equation of metabolites for flux estimation can be described by

$$\frac{d\mathbf{c}}{dt} = \mathbf{S}\mathbf{v}, \quad (2)$$

where  $\mathbf{c}$  is metabolite concentrations in the metabolic network, and  $\mathbf{S}$  is the stoichiometric matrix of the metabolic network. The integration of Equation (2) can be described by

$$\mathbf{c}(t) = \mathbf{c}_0 + \mathbf{S} \int_0^t \mathbf{v} dt. \quad (3)$$

Because  $\mathbf{v}$  is a vector of piecewise linear function of time, Equation (3) can be solved analytically. These equations were used to generate the graphs shown in Figure 2, Figure S2 and data in Table S2.

Equations for describing changes of mass isotopomer fractions over time under non-steady-state conditions

The elementary metabolite unit (EMU) framework (Antoniewicz et al., 2007; Young et al., 2008) was used to efficiently simulate mass isotopomer fractions (Figure 2, Figures S1 and S2). In EMU framework, a decomposition method is used to break isotopomers into EMUs to reduce computational burden. Each EMU includes a subset of metabolite atoms that are directly involved in precursor-product relationships. EMUs are organized into size blocks, for which size refers to the number of atoms included in the EMU. In EMU framework, mass isotopomer fractions of EMUs are sequentially simulated from smallest to largest size blocks.

Metabolic flux analyses using the EMU framework have been applied to metabolism under steady-state conditions (Young et al., 2008). Here, we developed an EMU framework that can be applied to metabolism under non-steady-state conditions. The EMU balance equations for  $n$ th size block under non-steady-state conditions can be expressed by

$$\frac{d \text{diag}(\mathbf{c}_n)\mathbf{x}_n}{dt} = \mathbf{A}_n\mathbf{x}_n + \mathbf{B}_n\mathbf{y}_n, \quad (4)$$

where  $\mathbf{x}_n$  is a vector of mass isotopomer fractions of EMUs.  $\mathbf{c}_n$  is a vector of concentrations corresponding to EMUs in  $\mathbf{x}_n$ , and  $\text{diag}(\mathbf{c}_n)$  is a diagonal matrix whose elements are  $\mathbf{c}_n$ .  $\mathbf{y}_n$  is a vector of mass isotopomer fractions of EMUs that are previously simulated inputs to the  $n$ th size block. Each EMU that comprises the  $\mathbf{x}_n$  and  $\mathbf{y}_n$  vectors is defined by the metabolite name and the subset of atoms it includes.  $\mathbf{A}_n$  and  $\mathbf{B}_n$  are functions of flux ( $\mathbf{v}$ ) and defined as follows:

$$\mathbf{A}_n(i, j) = \begin{cases} - \text{sum of fluxes consuming } i\text{th EMU in } \mathbf{x}_n, & i = j \\ \text{flux to } i\text{th EMU in } \mathbf{x} \text{ from } j\text{th EMU in } \mathbf{x}_n, & i \neq j \end{cases} \quad (5)$$

$$\mathbf{B}_n(i, j) = \text{flux to } i\text{th EMU in } \mathbf{x}_n \text{ from } j\text{th EMU in } \mathbf{y}_n. \quad (6)$$

Here, mass balance of metabolite concentrations corresponding to EMUs in  $\mathbf{x}_n$  can be described as follows:

$$\frac{d\mathbf{c}_n}{dt} = \mathbf{S}_n\mathbf{v}, \quad (7)$$

where  $\mathbf{S}_n$  is the stoichiometric matrix with each row representing the metabolite corresponding to EMUs in  $\mathbf{x}_n$ . By combining Equations (4) and (7), we can rewrite EMU balance equations:

$$\frac{d\mathbf{x}_n}{dt} = (\text{diag}(\mathbf{c}_n))^{-1}((\mathbf{A}_n - \text{diag}(\mathbf{S}_n\mathbf{v}))\mathbf{x}_n + \mathbf{B}_n\mathbf{y}_n). \quad (8)$$

We used Equation (8) to simulate mass isotopomer fractions of EMUs. Simulated mass isotopomer

fractions of a metabolite were obtained from the corresponding EMU with a size that is the same as the number of skeletal carbon atoms in the metabolite. Equation (8) was solved numerically using MATLAB function ode15s with absolute tolerance of  $5 \times 10^{-4}$ , relative tolerance of  $5 \times 10^{-4}$ , maximum order of formula of 3, and specified Jacobian sparsity pattern. Extracellular glucose was the only carbon source that uniformly labelled with  $^{13}\text{C}$  and was assumed to have atomic purity of 99%.

### Parameter estimation

Parameters  $\theta$  including switch times ( $t_1, t_2, \dots, t_K$ ), fluxes ( $v_k, k \in \{0, 1, \dots, K + 1\}$ ), and initial metabolite concentrations ( $c_0$ ) were estimated by minimizing the variance-weighted residual sum of squared errors (wRSS) between measured and simulated metabolite concentrations and mass isotopomer fractions according to the following equation (Figures 2 and 3, Figures S1 and S3):

$$\begin{aligned} \text{Min.}_{\theta} \quad & \text{wRSS} = (\mathbf{c}^{mes} - \mathbf{c})^T \Sigma_c^{-1} (\mathbf{c}^{mes} - \mathbf{c}) + (\mathbf{x}^{mes} - \mathbf{x})^T \Sigma_x^{-1} (\mathbf{x}^{mes} - \mathbf{x}), \\ \text{s. t.} \quad & \mathbf{c} \geq \mathbf{0}, \\ & \mathbf{c}_{0,\text{Ins}} = \mathbf{c}_{0,\text{Ctrl}}, \\ & \mathbf{v}_{0,\text{Ins}} = \mathbf{v}_{0,\text{Ctrl}}, \\ & \theta^{\text{LB}} \leq \theta \leq \theta^{\text{UB}}, \\ & t_{k+1} > t_k + \epsilon, \quad k \in \{0, 1, \dots, K\}, \end{aligned} \quad (9)$$

where  $\mathbf{c}^{mes}$  and  $\mathbf{x}^{mes}$  are vectors of the measured metabolite concentrations and mass isotopomer fractions, respectively (Data S1A).  $\Sigma_c$  and  $\Sigma_x$  are diagonal matrices containing measurement variances of metabolite concentrations and mass isotopomer fractions, respectively. To avoid overfitting of metabolite concentrations and mass isotopomer fractions that were associated with an unusually small standard deviation (SD), the minimum SD of the measured metabolite concentration was set at 1% and the minimum SD of the measured mass isotopomer fraction was set at 0.01.  $\mathbf{c}_{0,\text{Ins}}$  and  $\mathbf{c}_{0,\text{Ctrl}}$  are the initial metabolite concentrations in the Ins and Ctrl conditions, respectively, and set to be the same. Similarly,  $\mathbf{v}_{0,\text{Ins}}$  and  $\mathbf{v}_{0,\text{Ctrl}}$  are the initial fluxes in the Ins and Ctrl conditions, respectively, and set to be the same.  $\theta^{\text{LB}}$  and  $\theta^{\text{UB}}$  are lower and upper bounds of  $\theta$ , respectively (Data S1B).  $\epsilon$  was set to 1.01 to avoid  $t_k$  and  $t_{k+1}$  getting too close.

We obtained measured concentrations of mass isotopomers that were corrected for natural abundances from our previous paper (Krycer et al., 2017), and identified measured concentrations of mass isotopomers with amounts that were measured 2 or more times in 3 separate experiments. We calculated measured concentration of metabolite  $m$  ( $c_m^{mes}$ ) and measured fraction of mass isotopomer  $i$  of metabolite  $m$  ( $x_{m,i}^{mes}$ ) as follows:

$$c_m^{mes} = \sum_i d_{m,i}^{mes}, \quad (10)$$



$$x_{m,i}^{mes} = \frac{d_{m,i}^{mes}}{\sum_i d_{m,i}^{mes}}, \quad (11)$$

where  $d_{m,i}^{mes}$  is the measured concentration of mass isotopomer  $i$  of metabolite  $m$ . We also measured extracellular lactate and used this value for calculation of wRSS. Metabolites and mass isotopes used for calculating wRSS are shown in Data S1A. In total, we obtained 131 metabolite concentrations and 463 mass isotopomer fractions for the Ins condition, and 132 metabolite concentrations and 424 mass isotopomer fractions for the Ctrl condition.

The minimization problem of Equation (9) was numerically solved by a metaheuristic optimization of a covariance matrix adaptation evolution strategy (CMA-ES) with a negative update of the covariance matrix (Hansen and Kern, 2004) to approach the local minimum, followed by application of the interior point method to reach the local minimum using the MATLAB function `fmincon`. The initial population was sampled uniformly from the feasible region (Kaufman and Smith, 1998), and the mean and the covariance matrix were used as initial conditions for CMA-ES. The initial population size was set to  $10^3$  and the population size during the optimization was set to 50. The objective function of wRSS was evaluated at least  $1.5 \times 10^6$ . Parameter estimation was performed for 30 times with each number of time intervals to obtain the best parameter sets with minimized wRSS. Parameters were optimised in a logarithmic scale for CMA-ES and in a linear scale for `fmincon`.

### Introduction of quadratic programming during the metaheuristic optimization in the parameter estimation

Metabolic flux analysis under non-steady-state conditions requires more number of parameters and has a larger computation cost for optimization than metabolic flux analysis under steady-state conditions. We achieved faster optimization by introducing quadratic programming (QP) during the metaheuristic optimization (Figure S1E). Changes in metabolites concentrations can be described as piecewise quadratic functions as the integral of the piecewise linear functions of fluxes. Therefore, when independent parameters ( $\theta^{MO}$ ) including switch times are given, wRSS associated with only metabolite concentrations (wRSS<sup>QP</sup>) can be minimized easily by QP where variables are the remaining parameters ( $\theta^{QP}$ ):

$$\begin{aligned} \text{Min.}_{\theta^{QP}} \quad & \text{wRSS}^{QP} = (\mathbf{c}^{mes} - \mathbf{c})^T \Sigma_c^{-1} (\mathbf{c}^{mes} - \mathbf{c}), \\ \text{s. t.} \quad & \mathbf{c} \geq \mathbf{0}, \\ & \mathbf{c} = \mathbf{A}^{QP}(\theta^{MO}) \cdot \theta^{QP} + \mathbf{b}^{QP}(\theta^{MO}), \\ & \theta^{QP, LB} \leq \theta^{QP} \leq \theta^{QP, UB}, \end{aligned} \quad (12)$$

where  $A^{QP}$  and  $b^{QP}$  are a matrix and a vector, respectively, with elements that are determined from  $\theta^{MO}$ . We can identify which parameters are included in  $\theta^{MO}$  from Equation (9) before metaheuristic optimization. When  $t_k$  are given, all constraints in Equation (9) become linear. A basis for the row space of the coefficient matrix in the linear equality constraints corresponds to a parameter included in  $\theta^{QP}$ , whereas a non-basis corresponds to a parameter included in  $\theta^{MO}$ . Note that the initial metabolite concentrations ( $c_0$ ) were set to always be included in  $\theta^{MO}$ . During the metaheuristic optimization using CMA-ES, we iteratively perturbed the independent parameters  $\theta^{MO}$ , solved the QP problem in Equation (12) by the MATLAB function quadprog to obtain the other parameters  $\theta^{QP}$ , and evaluated wRSS in Equation (9). By introducing QP problem, we obtained parameter sets with the smallest wRSS values within a small number of evaluations of wRSS (Figure S1F), possibly because of the reduction in search space from the entire solution space during metaheuristic optimization.

#### Estimation of confidence intervals of parameters

Confidence intervals of parameters were estimated from the Jacobian matrix of the minimized wRSS. Assuming that the estimates of the minimization problem [Eq. (9)] converges to a global minimum, the Hessian matrix  $H$  can be approximated from the Jacobian matrix  $J$  as follows:

$$H = J^T J. \quad (13)$$

The Jacobian matrix includes the partial derivatives of wRSS with respect to the model parameters. We calculated the inverse of the Hessian, which gives the local estimate for the parameter covariance matrix  $\Sigma_\theta$ :

$$\Sigma_\theta = H^{-1}. \quad (14)$$

When we estimated fluxes using models for which the same number of time intervals was set among all reactions, confidence intervals of parameters were estimated based on linearized statistics as previously described (Antoniewicz et al., 2006). The diagonal elements of  $\Sigma_\theta$  are the variances of the estimated parameters, from which the approximated 90% confidence intervals (CI) can be calculated as

$$CI_i = \theta_i^* \pm z \sqrt{\Sigma_{\theta(i,i)}}, \quad (15)$$

where  $\theta^*$  is a vector of optimal estimates of the minimization problem [Eq. (9)], and  $z$  is the z-score for 90% confidence intervals (1.6449).

When we estimated fluxes using models under reaction-dependent number of time intervals, we sampled parameters for 200 times from a truncated multivariate normal distribution (Robert, 1995). The mean of the distribution was the optimal estimates of the minimization problem [Eq. (9)] and the

covariance matrix was  $\Sigma_{\theta}$ . The constraints of the distribution were the same as the minimization problem [Eq. (9)]. The sampled parameters are shown in Data S1C. The 90% confidence intervals of the parameters were calculated from the distribution of the sampled parameters. This calculation of the 90% confidence intervals accounts for constraints, such as the positive metabolite concentration, and for calculation of the confidence intervals of regulation coefficients, which are estimated in subsequent analyses. Because the confidence intervals were calculated from sampled parameters from a truncated multivariate normal distribution, the optimal estimates of parameters can be outside the confidence intervals due to the curse of dimensionality (Verleysen and François, 2005).

We understand that measured data are often perturbed by a Monte Carlo procedure to estimate confidence intervals of parameters in metabolic flux analysis (Hörl et al., 2013; Quek et al., 2020). However, applying a Monte Carlo procedure to our metabolic flux analysis would not be practical, because our metabolic flux analysis under non-steady-state conditions requires a large computational cost due to many number of parameters in optimization and many number of ODEs to be solved numerically. In our metabolic flux analysis, computational time of parameter estimation for one condition (e.g. experimental conditions and number of time intervals) was over 1.5 months on an AMD EPYC7501 processor on a Linux machine. Instead, we estimated confidence intervals of parameters from the inverse of the Hessian matrix of the minimized the variance-weighted residual sum of squared errors. The method we used is a general method to calculate confidence intervals in an approximate manner, and the computational cost is smaller than Monte Carlo procedures. We adopted appropriate methods of optimization and estimation of confidence intervals to match the complexity of our metabolic flux analysis under non-steady-state conditions.

#### Determination of reaction-dependent number of time intervals

Number of time intervals (or number of switch times) of fluxes should be selected for flux analysis under non-steady-state conditions (Figure 3, Figure S1). The number of time intervals cannot be selected by solving the optimization problem of Equation (9). More time intervals can potentially provide more accurate estimation of flux changes, which means smaller differences between measurements and estimates; however, more time intervals require more parameter numbers and less precise estimation, which means larger sensitivity to measurement errors.

Here, we propose a method to determine reaction-dependent number of time intervals, in which the number of time interval in each reaction can be independently determined (Figure S1C, D). First, we developed models in which the same number of time intervals was set among all

reactions, and estimated fluxes and their approximated confidence intervals as defined in Equation (15). The number of time intervals was either of one, two, or three. Next, we compared confidence intervals of each flux between models under one and two time interval(s). Because a higher number of time intervals may decrease estimation precision (as seen for Ogdh in Figure S1C), we selected the time interval of one for the reaction if confidence intervals for all time points were the same in models with one or two time intervals.

If confidence intervals for any time points were not the same for models with one or two time intervals, we tentatively selected two time intervals for the reaction because the lower number of time intervals may provide a less accurate estimation of flux changes (as seen for Pfk1 in Figure S1C). Reactions for which two time intervals are tentatively selected, we compared the confidence intervals for models with two or three time intervals and selected the number of time intervals using the same criterion that were used to select between one and two time intervals.

Because the confidence intervals used to determine the number of time intervals depend on z-score (or percentage for the confidence intervals), we generated 10 models using different z-scores for the calculation of the confidence intervals. Smaller z-scores lead to narrower confidence intervals and result in models with a larger number of parameters. We performed metabolic flux analysis using each of the generated models and selected the model with the smallest AIC as the final model with a reaction-dependent number of time intervals. The AIC value of the final model is smaller than the any of the models with the same number of time intervals among all reactions (Figure S1D), indicating that the model with a reaction-dependent number of time intervals is statistically more appropriate than models with the same number of time intervals among all reactions. This method reduced computation cost compared to methods for selecting time intervals from all possible combinations of the number of time intervals.

#### Estimation of glucose uptake, <sup>14</sup>C-glycogen accumulation, <sup>14</sup>C-fatty acid accumulation in TG and <sup>14</sup>C- CO<sub>2</sub> secretion

To validate the estimated flux from other experiments using natural glucose or <sup>14</sup>C-glucose as a tracer (Figure 4), we estimated glucose uptake, <sup>14</sup>C-glycogen accumulation, <sup>14</sup>C-fatty acid accumulation in TG, and <sup>14</sup>C-CO<sub>2</sub> secretion using the model and the estimated fluxes. These estimates were calculated using the estimated flux  $v$  through reaction  $j$  from substrate  $k$  to product  $l$  and the estimated fractions of  $M+i$  mass isotopomer of a substrate  $k$ :

$$-n_k \cdot S_{k,j} \cdot r_{j,k,l} \int_0^{60} v_j(t) \frac{\sum_{i=0}^{n_k} i \cdot x_{k,i}(t)}{n_k} dt, \quad (16)$$

where  $n_k$  is the number of skeletal carbon atoms in substrate  $k$ .  $S_{k,j}$  is the stoichiometric coefficient of substrate  $k$  in reaction  $j$  and is a negative value.  $r_{j,k,l}$  is the ratio of carbon atoms in substrate  $k$  that is transferred to product  $l$  through reaction  $j$ .

For glucose uptake, the substrate is extracellular glucose, the product is intracellular glucose, and the reaction is Glut4. For  $^{14}\text{C}$ -glycogen accumulation, the substrate is UDP-glucose, the product is glycogen, and the reaction is Gys. For  $^{14}\text{C}$ -fatty acid accumulation in TG, the substrate is Cit\_Acon\_IsoCit, the product is TG, and the reaction is Gpat\_Acly. For  $^{14}\text{C}$ - $\text{CO}_2$  secretion, the substrate is the intracellular  $\text{CO}_2$ , the product is the extracellular  $\text{CO}_2$ , and the reaction is the  $\text{CO}_2$  transporter (CO2t).  $r_{j,k,l}$  is 0.33 for  $^{14}\text{C}$ -fatty acid accumulation in TG and 1 for the others.

### **Identification of key regulatory mechanisms in the glucose metabolism in insulin-stimulated adipocytes**

An overview of the description of flux based on reaction kinetics is shown in Figure 5A. In addition to substrates and products, we included enzyme phosphorylation and allosteric effectors that can potentially regulate fluxes in addition to substrates and products. We obtained enzyme phosphorylation results that were classified as Class I (a phosphorylation site localization probability score derived from MaxQuant (Cox and Mann, 2008)  $> 0.75$ ) in phosphoproteomic data (Humphrey et al., 2013). We obtained information of reported allosteric effectors for *Mus musculus*, *Rattus norvegicus*, and *Homo sapiens* in the BRENDA database using the Simple Object Access Protocol (SOAP) with Perl (Placzek et al., 2017). We obtained the amounts of phosphorylation and allosteric effectors from phosphoproteomic and metabolomics data in previous studies (Humphrey et al., 2013; Krycer et al., 2017), respectively, and identified enzyme phosphorylation and allosteric effectors with amounts that were measured 2 or more times in 3 separate experiments. In total, 82 phosphorylation sites (80 unique sites on 25 enzymes) and 170 allosteric effectors together with substrates and products were obtained as candidates of regulatory molecule (Table S3).

#### Reaction kinetic equation

We developed models for each reaction in which flux is described as a modular rate law (Liebermeister et al., 2010) (Figure 5A). We used common modular with complete activation or inhibition and we set all relevant regulation numbers to a value of one, assuming no cooperativity. In the model selection, we develop a model containing  $k_1$  and only a function of substrate and products, and we also develop models containing one or more functions of enzyme phosphorylation

and allosteric effectors, as well as  $k_1$  and the function of substrates and products. For each reaction, flux  $v^{kinetic}$  is defined as a product of kinetic constant  $k_1$  and functions of amounts of substrates and products, enzyme phosphorylation, and allosteric effectors:

$$v^{kinetic} = k_1 \cdot f_S \cdot \prod_{i \in U_P} f_{P,i} \cdot \prod_{j \in U_A} f_{A,j}, \quad (17)$$

$$f_S = \frac{\prod(c_S/K_S) - k_2 \prod(c_P/K_P)}{\prod(1 + c_S/K_S) + \prod(1 + c_P/K_P) - 1}, \quad (18)$$

$$f_{P,i} = \begin{cases} \frac{P_i}{K_{PE,i} + P_i}, & \text{if } i\text{-th enzyme phosphorylation is an activator,} \\ \frac{K_{PE,i}}{K_{PE,i} + P_i}, & \text{if } i\text{-th enzyme phosphorylation is an inhibitor,} \end{cases} \quad (19)$$

$$f_{A,j} = \begin{cases} \frac{C_{A,j}}{K_{A,j} + C_{A,j}}, & \text{if } j\text{-th allosteric effector is an activator,} \\ \frac{K_{A,j}}{K_{A,j} + C_{A,j}}, & \text{if } j\text{-th allosteric effector is an inhibitor,} \end{cases} \quad (20)$$

where  $f_S$  is a function of substrate and products (generalized Michaelis-Menten kinetics).  $U_P$  and  $U_A$  are the sets of candidate enzyme phosphorylation and allosteric effectors, respectively, that affect the flux as activators or inhibitors and the union of  $U_P$  and  $U_A$  is defined as  $U$ .  $f_{P,i}$  is a function of  $i$ -th enzyme phosphorylation. Enzyme phosphorylation was considered for both cases of either an activator or an inhibitor.  $f_{A,j}$  is a function of  $j$ -th allosteric effector. Allosteric effectors were considered as activators or inhibitors according to information in BREDNA database (Placzek et al., 2017).  $c_S$ ,  $c_P$ , and  $c_A$  are amounts of the substrate, product, and allosteric effector, respectively, and their amounts were obtained from metabolomics data (Krycer et al., 2017) otherwise from estimated amounts of metabolites in our metabolic flux analysis. Note that summed metabolites in the metabolic flux analysis were separated in this analysis (for example, G6P\_F6P was separated into G6P and F6P) and separated amounts were used for  $c_S$  and  $c_A$ . F1,6BP and F2,6P were summed as FBP in the metabolic flux analysis. Here, we measured F1,6BP and F2,6BP separately by IC-MS and the amount of each of F1,6BP and F2,6BP were used for  $c_S$  and  $c_A$ . 3PG and 2PG can not be separated by our measurement condition and only summed amounts ( $c_{3PG,2PG}$ ) were available. We assumed 3PG and 2PG were close to equilibrium and we calculated separate amounts of 3PG ( $c_{3PG}$ ) and 2PG ( $c_{2PG}$ ) from  $c_{3PG} + c_{2PG} = c_{3PG,2PG}$  and  $c_{2PG}/c_{3PG} = K_{eq}$ , where  $K_{eq}$  is 5.38 at pH = 7.2 and ionic strength = 0.15 M (Haraldsdóttir et al., 2012) according to eEquilibrator (Noor et al., 2013).  $P_i$  is an amount of  $i$ -th phosphorylation at a site of an enzyme. Amounts of

enzyme phosphorylation in the Ins condition were obtained from phosphoproteomic data in adipocytes in our previous study (Humphrey et al., 2013), while amounts of enzyme phosphorylation in the Ctrl conditions were set equal to the amount of enzyme phosphorylation at 0 min.  $k_1$  and  $k_2$  are kinetic constants.  $K_S$ ,  $K_P$ ,  $K_{PE}$  and  $K_A$  are affinity constants for the substrate, product, enzyme phosphorylation and allosteric effectors, respectively. We assumed that enzyme amounts remain constant and can be included in  $k_1$ , because our carbon labelling experiments (60 min) was much shorter than 31 hours of median half-life of proteins (Sandoval et al., 2013).  $c_S$ ,  $c_P$ ,  $c_A$  and  $P$  were normalized by the  $L^2$  norm before the following parameter estimation.

### Parameter estimation

Kinetic parameters  $\theta^{kinetic}$ , including  $k_1, k_2, K_S, K_P, K_{PE}$  and  $K_A$ , were estimated for each reaction using each model by minimizing the residual sum of squared errors (RSS) between fluxes defined by the modular rate law and the fluxes estimated by metabolic flux analysis in a logarithmic scale (Figure 5A):

$$\underset{\theta^{kinetic}}{\text{Min.}} \text{ RSS} = (\log \mathbf{v}' - \log \mathbf{v}^{kinetic}(\theta^{kinetic}))^T (\log \mathbf{v}' - \log \mathbf{v}^{kinetic}(\theta^{kinetic})), \quad (21)$$

where  $\mathbf{v}'$  is the fluxes estimated by metabolic flux analysis and is normalized by the  $L^2$  norm. RSS was calculated from data at 1, 5, 10, 20, and 60 min, which is the shared time points between metabolomic and phosphoproteomic data in the Ins and Ctrl conditions. The minimization problem of Equation (21) was numerically solved by CMA-ES with a negative update of the covariance matrix, followed by interior point method using MATLAB function `fmincon` as applied to our metabolic flux analysis. The population size and the maximum number of RSS evaluations in CMA-ES was set to 30 and  $10^4$ , respectively. Parameter estimation was performed five times to obtain the best parameter sets with minimized RSS for each reaction using each model.

### Model selection

Because not all enzyme phosphorylation and allosteric effectors effectively change the enzymatic activity and regulate fluxes, we identified enzyme phosphorylation and allosteric effectors that, together with substrates and products, effectively regulated fluxes using model selection (Figure 5A). We used AIC as the selection criterion for the model selection:

$$\text{AIC} = N \log \frac{\text{RSS}}{N} + 2p, \quad (22)$$

where  $N$  is the number of residuals and  $p$  is the number of kinetic parameters in the model. We performed model selection to determine  $U (=U_P \cup U_A)$  using a stepwise selection method based on

AIC according to the following procedure (Yamashita et al., 2007):

(i) Set the subset  $U$  as an empty set, estimate the set of parameters that minimizes RSS, and calculate AIC. Here,  $U$  is temporarily set as the subset that minimizes AIC. Hereafter, we denoted the complementary set of  $U$  as  $U^c$ , and the size of the subset  $U$  as  $\#U$ .

(ii) For each candidate regulatory molecule  $i$  in  $U^c$ , add the  $i$  to  $U$  (denoted as  $U_i$ ), estimate the set of parameters that minimizes RSS, and calculate AIC [denoted as  $AIC(U_i)$ ].

(iii) Select  $U^* = \underset{U_i}{\operatorname{argmin}} AIC(U_i)$  from  $\#U^c$  candidates defined in step (ii). If  $AIC(U) > AIC(U^*)$ ,

update  $U$  with  $U^*$ . If  $AIC(U) \leq AIC(U^*)$ , go to step (vi).

(iv) For each regulatory molecule  $j$  in  $U$ , remove the  $j$  from  $U$  (denoted as  $U_j$ ), estimate the set of parameters that minimizes RSS, and calculate AIC [denoted as  $AIC(U_j)$ ].

(v) Select  $U^* = \underset{U_j}{\operatorname{argmin}} AIC(U_j)$  from  $\#U$  candidates defined in step (iv). If  $AIC(U) > AIC(U^*)$ ,

update  $U$  with  $U^*$ , and go to step (iv). If  $AIC(U) \leq AIC(U_j)$ , go to step (ii).

(vi) stop stepwise method.

We qualitatively identified the regulatory molecules in the final  $U$  with the smallest AIC. This model selection was performed for each reaction independently. The estimated parameters are shown in Data S1D.

### Calculation of regulation coefficients

To quantify contributions of regulatory events by substrates, products, and the selected enzyme phosphorylation, or allosteric effectors, as well as unaccounted regulators to the estimated flux differences between the Ins and Ctrl conditions, we calculated a regulation coefficient  $\rho$  (Figure 5A). Similar approaches have been reported in previous studies (Gerosa et al., 2015; Hackett et al., 2016; ter Kuile and Westerhoff, 2001). Using the estimated kinetic parameters, the normalized flux estimated by metabolic flux analysis can be described for each point in each reaction as follows:

$$v' = k_1 \cdot f_S \cdot \prod_i f_{P,i} \cdot \prod_j f_{A,j} \cdot f_U, \quad (23)$$

where  $f_U$  is  $v'/v^{kinetic}$ , calculated from a residual in Equation (21). Variance of the fluxes in a logarithmic scale between the Ins and Ctrl conditions can be written as follows:

$$\sigma_{\log v}^2 = \left( \frac{\partial \log v'}{\partial \log \mathbf{f}} \right)^T \Sigma_{\log f} \left( \frac{\partial \log v'}{\partial \log \mathbf{f}} \right), \quad (24)$$



where  $\sigma_{\log v}^2$  is the variance of the fluxes at a logarithmic scale.  $\mathbf{f}$  is a vector of  $f_S$ ,  $f_P$ ,  $f_A$ , and  $f_U$ , and  $\Sigma_{\log f}$  is the covariance matrix of  $\log \mathbf{f}$  and the diagonal elements of  $\Sigma_{\log f}$  is the variance of  $\log \mathbf{f}$  ( $\sigma_{\log f}^2$ ) between the Ins and Ctrl conditions. According to Equation (23), the partial derivative of  $\log v'$  with respect to each  $\log f$  equals to one. We made the simplifying assumption that covariance between  $\log \mathbf{f}$  is negligible and therefore  $\Sigma_{\log f}$  is diagonal:

$$\sigma_{\log v}^2 \approx \sum \sigma_{\log f}^2. \quad (25)$$

We defined a regulation coefficient  $\rho$  as the contribution of each of identified enzyme phosphorylation and allosteric effectors, substrates and products, and unaccounted regulators to the flux difference between the Ins and Ctrl conditions, which is calculated by normalizing  $\sigma_{\log f}^2$  at each time in Equation (25):

$$\rho = \frac{\sigma_{\log f}^2}{\sum \sigma_{\log f}^2}. \quad (26)$$

A regulation coefficient can take values from zero to one. Here, the variance between two conditions of Ins and Ctrl ( $\sigma_{\log f}^2$ ) can be written by the difference between the two conditions ( $\Delta \log f$ ):

$$\sigma_{\log f}^2 = \left( \frac{\Delta \log f}{2} \right)^2. \quad (27)$$

By combining Equations (26) and (27), we can rewrite regulation coefficients:

$$\left\{ \begin{array}{l} \rho_{P,i} = \frac{(\Delta \log f_{P,i})^2}{\sum (\Delta \log f)^2}, \\ \rho_{A,j} = \frac{(\Delta \log f_{A,j})^2}{\sum (\Delta \log f)^2}, \\ \rho_S = \frac{(\Delta \log f_S)^2}{\sum (\Delta \log f)^2}, \\ \rho_U = \frac{(\Delta \log f_U)^2}{\sum (\Delta \log f)^2}, \end{array} \right. \quad (28)$$

where  $\rho_{P,i}$  stands for contribution of phosphorylation at site  $i$  to the flux difference between the Ins and Ctrl conditions and summation of  $\rho_{P,i}$  for each reaction at each time point is denoted as  $\rho_P$ .  $\rho_{A,j}$  stands for contribution of allosteric effector  $j$ , and summation of  $\rho_{A,j}$  is denoted as  $\rho_A$ .  $\rho_S$ , and  $\rho_U$  stand for contributions of substrates and products, and unaccounted regulators, respectively. We calculated regulation coefficients at 1, 5, 10, 20, and 60 min, which are the same as the time points used for the kinetic parameter estimation. We linearly interpolated the regulation coefficients between the time points, and calculated a time-averaged regulation coefficient by the following:

$$\text{time-averaged } \rho = \frac{\int_1^{60} \rho(t) dt}{\int_1^{60} dt}. \quad (29)$$

#### Estimation of confidence intervals of regulation coefficients

To estimate confidence intervals of regulation coefficients (Figure 6A, Figures S4 and S5), we used the sampled parameters for the estimation of confidence intervals in the metabolic flux analysis (Data S1C). For each reaction in each sampling, we performed kinetic modelling with model selection and calculated the regulation coefficients. Amounts of enzyme phosphorylation were sampled from a normal distribution with a mean and a variance from the phosphoproteomic data (Humphrey et al., 2013). Amounts of allosteric effectors, substrates, and products were obtained from a normal distribution with a mean and a variance from the metabolomics data (Krycer et al., 2017); otherwise the amounts were from the sampled parameters. We identified the regulatory molecules in the model finally selected (Table S3) and calculated regulation coefficients using each set of the sampled or obtained amounts of enzyme phosphorylation, allosteric effectors, substrates, and products, as well as the fluxes (Table S4). The 90% confidence intervals of regulation coefficients including  $\rho_P$ ,  $\rho_A$ ,  $\rho_S$ , and  $\rho_U$  were calculated from the distribution of the regulation coefficients.

#### Determination of key regulatory molecules

Reactions with the 90% confidence interval of time-averaged  $\rho$  above zero were further analysed to determine key regulatory molecules in glucose metabolism in insulin-stimulated adipocytes. We focused on how many times each regulatory molecule was selected among 200 model selections using sampled parameters, and regarded the most selected regulatory molecules for each reaction as the key regulatory molecule that represent flux through the reaction.

#### Michaelis-Menten constants from the BRENDA database

Michaelis-Menten constants were obtained from the BRENDA database (Placzek et al., 2017) based on EC numbers. The Perl implementation of the Simple Object Access Protocol (SOAP::Lite) was employed to extract the  $K_M$  values in *Mus musculus*, *Rattus norvegicus*, *Homo sapiens*, *Bos taurus*, *Sus scrofa*, *Canis lupus familiaris*, and *Mammalia*. The exported data were further processed to remove entries for mutant enzymes.  $K_M$  values with three or more reports for a substrate or a product of a reaction were selected (Data S1E), and the geometric mean and the geometric standard deviations were calculated and compared with estimated values (Figure S4B).

## **Experimental methods**

### **Metabolomic and phosphoproteomic data in insulin-stimulated adipocytes**

For metabolic flux analysis and key regulatory mechanisms, we used metabolomic and phosphoproteomic data from insulin-stimulated adipocytes in our previous studies (Humphrey et al., 2013; Krycer et al., 2017; Quek et al., 2020) and the experimental procedures of the previous studies are briefly described below. For metabolomic measurements (Krycer et al., 2017; Quek et al., 2020), differentiated 3T3-L1 adipocytes were labelled with [U-<sup>13</sup>C] glucose (25 mM, 99 atom % <sup>13</sup>C) and treated with 100 nM insulin or vehicle (PBS) for 1, 5, 10, 20, 40, or 60 min. Labelling with <sup>13</sup>C and the treatment with 100 nM insulin or vehicle were started at the same time. Cell lysates and the culture media were analysed by CE-MS and liquid chromatography-mass spectrometry (LC-MS), respectively. For phosphoproteomic measurements (Humphrey et al., 2013), 3T3-L1 fibroblasts were triple SILAC labelled, differentiated into adipocytes, and treated with 100 nM insulin or vehicle (PBS) for 15 s, 30 s, 1 min, 2 min, 5 min, 10 min, 20 min, or 60 min. Proteins were acetone precipitated, resuspended in urea, reduced, alkylated, and digested with endoproteinase Lys-C followed by trypsin. Peptides were desalted and fractionated by strong cation exchange (SCX) and TiO<sub>2</sub> for phosphopeptide analysis. Eluted peptides were analysed by quantitative mass spectrometry.

### **Measurement of F1,6BP and F2,6BP by IC-MS**

We measured F1,6BP and F2,6BP in the same samples of our previous study (Krycer et al., 2017). Capillary IC-MS analysis was performed using a Dionex ICS-5000+ system equipped with a Q Exactive Orbitrap MS system (Thermo Fisher Scientific, San Jose, CA) (Hirayama et al., 2020). The IC system consisted of a capillary pump, an eluent generator with a capillary KOH cartridge, an anion capillary electrolytic suppressor (ACES 300), and a conductivity detector. Ultrapure water was used as both the eluent and regenerant in the suppressor. Sample injection was performed with a Dionex WPS-3000TBPL autosampler. An Agilent 1100 series capillary HPLC pump (Agilent Technologies Deutschland GmbH, Waldbronn, Germany) was used to deliver the make-up solution.

Anionic metabolites were separated on a Dionex IonPac AS11-HC-4 µm column (250 × 0.4 mm, 4 µm; Thermo Fisher Scientific) that was maintained at 35°C. The flow rate was 20 µL/min and the injection volume was 0.4 µL. The following KOH concentration gradient was used: 1 mmol/L from 0 min to 2 min, 20 mmol/L at 16 min, 100 mmol/L at 35 min, held at 100 mmol/L until 40 min, and then

decreased to the initial concentration within 0.1 min and held at this concentration for 5 min. The total analysis time was 45.1 min. Isopropanol containing 0.1% acetic acid was delivered as the make-up solution at 5  $\mu$ L/min.

The standard ESI sprayer (product number OPTON–20011, Thermo Fisher Scientific), without any alterations, was used in this study. The standard ESI sprayer contains two coaxial tubes. A fused-silica capillary (0.10 mm I.D., 0.19 mm O.D.), through which the eluent flowed, was inserted in a stainless-steel tube with a slightly larger diameter (first tube). A make-up solution was supplied through this tube and mixed with the eluent at the outlet of the sprayer. In addition, the sheath gas which assists with stable spray formation was supplied from the second coaxial tube.

The Q Exactive mass spectrometer was operated in ESI negative ion mode and the spray voltage was set at 4.0 kV. The capillary temperature was 300 °C, the sheath gas flow rate was 20 (arbitrary units), the auxiliary gas flow rate was 10 (arbitrary units), the sweep gas flow rate was 0 (arbitrary units), and the S-lens was 50 (arbitrary units). Full scan mode was used and the parameters were as follows: resolution, 70,000; auto gain control target,  $1 \times 10^6$ ; maximum ion injection time, 100 ms; and scan range, 70–1000 m/z. The instrument was calibrated at the beginning of each sequence using the calibration solution provided by the instrument manufacturer.

### **Quantification and statistical analysis**

All statistical details including statistical tests used, exact value of n, what n represents, definition of centre, and dispersion measures are described in the figure legends.

## SUPPLEMENTAL REFERENCES

- Antoniewicz, M.R., Kelleher, J.K., and Stephanopoulos, G. (2006). Determination of confidence intervals of metabolic fluxes estimated from stable isotope measurements. *Metab. Eng.* 8, 324–337.
- Antoniewicz, M.R., Kelleher, J.K., and Stephanopoulos, G. (2007). Elementary metabolite units (EMU): A novel framework for modeling isotopic distributions. *Metab. Eng.* 9, 68–86.
- Body, D.R. (1988). The lipid composition of adipose tissue. *Prog. Lipid Res.* 27, 39–60.
- Cherrington, A.D. (1999). Banting Lecture 1997. Control of glucose uptake and release by the liver in vivo. *Diabetes* 48, 1198–1214.
- Cox, J., and Mann, M. (2008). MaxQuant enables high peptide identification rates, individualized p.p.b.-range mass accuracies and proteome-wide protein quantification. *Nat. Biotechnol.* 26, 1367–1372.
- Hansen, N., and Kern, S. (2004). Evaluating the CMA Evolution Strategy on Multimodal Test Functions. (Springer, Berlin, Heidelberg), pp. 282–291.
- Haraldsdóttir, H.S., Thiele, I., and Fleming, R.M.T. (2012). Quantitative assignment of reaction directionality in a multicompartmental human metabolic reconstruction. *Biophys. J.* 102, 1703–1711.
- Hörl, M., Schnidder, J., Sauer, U., and Zamboni, N. (2013). Non-stationary <sup>13</sup>C-metabolic flux ratio analysis. *Biotechnol. Bioeng.* 110, 3164–3176.
- Kaufman, D.E., and Smith, R.L. (1998). Direction Choice for Accelerated Convergence in Hit-and-Run Sampling. *Oper. Res.* 46, 84–95.
- ter Kuile, B.H., and Westerhoff, H. V (2001). Transcriptome meets metabolome: hierarchical and metabolic regulation of the glycolytic pathway. *FEBS Lett.* 500, 169–171.
- Leighty, R.W., and Antoniewicz, M.R. (2011). Dynamic metabolic flux analysis (DMFA): a framework for determining fluxes at metabolic non-steady state. *Metab. Eng.* 13, 745–755.
- Noor, E., Haraldsdóttir, H.S., Milo, R., and Fleming, R.M.T. (2013). Consistent Estimation of Gibbs Energy Using Component Contributions. *PLoS Comput. Biol.* 9.
- Robert, C.P. (1995). Simulation of truncated normal variables. *Stat. Comput.* 5, 121–125.
- Sandoval, P.C., Slentz, D.H., Pisitkun, T., Saeed, F., Hoffert, J.D., and Knepper, M.A. (2013). Proteome-wide measurement of protein half-lives and translation rates in vasopressin-sensitive collecting duct cells. *J. Am. Soc. Nephrol.* 24, 1793–1805.
- Young, J.D., Walther, J.L., Antoniewicz, M.R., Yoo, H., and Stephanopoulos, G. (2008). An elementary metabolite unit (EMU) based method of isotopically nonstationary flux analysis. *Biotechnol. Bioeng.* 99, 686–699.